PROCESSING BETA-TRICALCIUM PHOSPHATE AND 45S5 BIOGLASS MIXTURES FOR OSTEOGENIC BONE TISSUE SCAFFOLDS

by

PHILLIP ZACHARY JAMES

Presented to the Faculty of the Graduate School of

The University of Texas at Arlington in Partial Fulfillment

of the Requirements

for the Degree of

MASTER OF SCIENCE IN MATERIAL SCIENCE AND ENGINEERING

THE UNIVERSITY OF TEXAS AT ARLINGTON

AUGUST 2017

ACKNOWLEDGEMENTS

I would like to thank both Dr. Panos S. Shiakolas and Dr. Pranesh B. Aswath for their guidance throughout this research. And I would like to thank the committee member Dr. Venu G. Varanasi.

This thesis would not have been possible without Prashanth Ravi and Anabelle (Chen-Ning) Yao, whose help was invaluable.

The beamtime for XANES testing was provided by the Canadian Light Source in Saskatoon, Canada, which is supported by NSERC, NRC, CIHR, and the University of Saskatchewan. I would also like to thank Vinay Sharma and Tugba Cebe from UTA who ran the XANES tests in Canada.

I would like to thank the following people at UTA for their contributions. Kermit Beird and Sam Williams in the MAE machine shop ground the bulk compression test samples and fabricated the molds. Dr. Yuriy Nikishkov performed the CT scans on the laponite samples. I would also like to thank both Dr. Felipe Monte and the members of the MARS lab for their general support.

Much of the testing was performed in the UTA Characterization Center for Materials and Biology (CCMB) and I would like to thank the lab for their support.

I would like to thank the following people from industry for their advice and/or small donations: John Titone at Nordson EFD Inc, Dr. Shannon Morrison at BYK additives, and Les Shawber at Grace Materials Technologies.

July 28, 2017

ABSTRACT

PROCESSING BETA-TRICALCIUM PHOSPHATE AND 45S5 BIOGLASS MIXTURES FOR OSTEOGENIC BONE TISSUE SCAFFOLDS

Phillip Zachary James, M.S.

The University of Texas at Arlington, 2017

Supervising Professor: Panos Shiakolas

A 30% 45S5 Bioglass and 70% β-tricalcium phosphate ceramic mixture, which was previously shown to be osteogenic [1], was sintered and the process was investigated as a strengthening mechanism. Samples were sintered for dwell times of 1, 2, and 4 hrs at 500°C to avoid crystallization of the 45S5 Bioglass. Two different binders were used, 2% gelatin in deionized water and 2% laponite with 2% oleic acid in deionized water. The mixture was also robocasted as a slurry to evaluate the manufacturing process.

Mechanical compression testing shows that the laponite with oleic acid binder acted as a sintering aid leading to a small increase in strength with longer sintering times, while the 2% gelatin binder had no clear trend in strength increase. Computed X-ray tomography (μ-CT) scans revealed no significant densification from the sintering process and scanning electron microscope (SEM) images revealed no significant changes in the microstructure which indicates that 500°C is an ineffective sintering temperature.

X-ray absorption near edge structure (XANES) analysis was performed for silicon and phosphorus $L_{2,3}$-edges and for oxygen K-edge. Silicon $L_{2,3}$-edge data reveals that for the laponite with oleic acid binder samples, longer sintering times change the spin-orbit interaction of the 2p electrons as the bonding structure becomes more similar to sodium silicate and the laponite becomes incorporated into the SiO_2 glass network. Phosphorous $L_{2,3}$-edge data reveals no significant changes in phosphate bonding structure which is to be expected.

It is known that for the $Na_2O - CaO - SiO_2$ system that non-bridging oxygen atoms preferentially bond to Ca instead of Na. The oxygen K-edge data shows that the samples have an increase in bridging oxygen bonds (Si-O-Si) over 45S5 Bioglass, which indicates that after addition of the binder, there is a decrease in the amount of Na in the glass network relative to Ca. The bridging oxygen bonding decreases upon sintering but there are no significant changes for longer sintering times.

For robocasting of the ceramic slurry, an engineering case study is presented to discuss issues related to process repeatability, lessons learned in implementing the process, and suggestions for future work.

TABLE OF CONTENTS

LIST OF ILLUSTRATIONS

LIST OF TABLES

LIST OF ABBREVIATIONS

AM	Additive Manufacturing
ASTM	American Society for Testing and Materials International
BG	45S5 Bioglass™
BO	Bridging Oxygen
CDHA	Calcium Deficient Hydroxyapatite
CT	X-ray Computed Tomography
ECM	Extra-Cellular Matrix
FY	Fluorescence Yield
G	Gelatin Binder
HA	Hydroxyapatite or Hydroxylapatite (alternate spelling)
L	Laponite and Oleic Acid Binder
LH	Layer Height
MBG	Mesoporous Bioactive Glass
NBO	Non-Bridging Oxygen
P/L	Powder to liquid ratio (g per mL)
PBS	Dulbecco's Phosphate Buffered Saline
SEM	Scanning Electron Microscope
TCP	Tricalcium Phosphate
TEY	Total Energy Yield
TGA	Thermogravimetric Analysis
XANES	X-ray absorption near-edge structure
XRD	X-ray Diffraction

CHAPTER 1

Introduction and Background

1.1 Need of Biomaterials for Bone Grafting and Bone Tissue Engineering

A widely quoted figure estimates that 500,000 bone graft procedures are performed in the United States each year [4]. A more in depth analysis of the U.S. National Hospital Discharge Survey between 1992 and 2007 shows that of almost 2 million bone graft procedures performed, 83% were autogenous and 17% were either allografts or artificial [5].

Biological sources for bone graft material are autogenous/autografts (from patient), allografts (from cadaver), and xenografts (from animal). Autografts require additional surgery with potential complications from donor site morbidity. Allografts and xenografts are potentially immunogenic which can lead to rejection of the transplanted tissue.

Synthetic materials for medical implantation, despite being bioinert will still cause a foreign body response that can hinder tissue function. The foreign body response is initiated when the surface chemistry of a material causes proteins to denature as they are adsorbed onto the material surface. The denatured proteins initiate a response from macrophage cells which eventually leads to the growth of a layer of fibrotic tissue surrounding the implanted material [6]. These problems have lead to the development of bio-active materials that are able to integrate with tissue and either bioresorb or biodegrade over time. Bioresorbable materials show bulk degradation and further resorb in vivo eventually leading to total elimination from

the body. Biodegradable materials break down and disperse in vivo and may move away from the initial site but are not completely eliminated from the body [7].

In conjunction with biomaterials research, tissue engineering is an active research area. The goal of tissue engineering is to provide proper signals to stem cells to induce the proliferation of stem cells, differentiation of stem cells into the appropriate cell type, and regeneration of fully functional tissue. Current methods being studied involve creating a porous structure called a scaffold which functions as the extracellular matrix (ECM) which is then seeded with stem cells and implanted in the body. The scaffold provides mechanical support during tissue regrowth while providing signals to the cells through its surface chemistry, topology of its micro and nano-scale structure, mechanical response, etc.

One of the many challenges facing tissue engineering is control of the scaffold pore structure. The scaffold needs to be porous to allow space for cell in-growth, vascularization, and for nutrient and oxygen transport to ensure cell survival. For bone tissue, the optimum pore size is disputed and studies have used pore sizes from 20 to 1500 μm [8]. Scaffolds with a gradient of pore sizes from 750 μm to 100 μm have been shown to increase cell seeding efficiencies from 35% to 70% when compared to scaffolds with a single pore size [9]. Traditional scaffold fabrication techniques include solvent casting/particulate leaching, gas foaming, fiber bonding, electrospinning, and phase separation methods. These traditional methods create highly porous scaffolds, but have little direct control over either the pore structure, size, and/or inter-connectivity while additive manufacturing methods have the advantage of precisely controlling the pore size and inter-connectivity [8].

1.2 Previous Research

This current research is a continuation and extension of research performed by Chien-Ning Yao (Anabelle) for her master's thesis while she was in this research group. Initial material testing and in vitro testing with MC3T3-E1 cells was performed using two powder compositions: 20% 45S5 Bioglass+80% β-TCP and 30% 45S5 Bioglass + 70% β-TCP and using three different binders in deionized water: 2% gelatin, 2% laponite, and 2% Na_2HPO_4 [1].

The 30% 45S5 Bioglass + 70% β-TCP mixtures compared to the 20% Bioglass mixtures had slightly improved cell viability and proliferation but significantly higher compression strength. While the mixtures with 2% Na_2HPO_4 binder had comparable in vitro results for cell viability and proliferation, their injectability was poor which makes the binder unsuitable for robocasting. Therefore, this current research focuses on using 30% 45S5 Bioglass + 70% β-TCP as the powder and two different binders: 2% gelatin and 2% laponite.

For the 30% Bioglass + 70% β-TCP powder mixture, initial compression testing was performed on unsintered bulk samples after soaking the samples in PBS for 1 day and 28 days. Results showed that when soaked in PBS for 28 days the bulk samples had a compression strength of 8.22 MPa with the 2% gelatin binder and 5.08 MPa with the 2% laponite binder. The 28 day strengths are similar to trabecular bone (6.17 MPa). But at a 1 day PBS soak time, the bulk samples had a compression strength of only 1.53 MPa with the 2% gelatin binder and 0.809 MPa the 2% laponite binder, which is obviously problematic.

1.3 Bone Composition and Biological Apatites

The ECM of bone tissue is a polymer matrix-ceramic composite with a hierarchical structure all the way down to the nanoscale. Bone composition by weight is approximately 65% mineral, 10% water, and 20-25% organic components 90% of which is type I collagen [10].

Bone mineral is often assumed to be hydroxyapatite, ($Ca_{10}(PO_4)_6(OH)_2$), but in dentin and bone mineral there are frequent substitutions of CO_3^{2-} ions at disordered PO_4^{3-} crystal lattice sites and substitutions of several different ionic species at the Ca^{2+} lattice sites. Also, biological apatites are non-stochiometric mixtures and may have Ca/P molar ratios between 1.5 and 1.66 versus Ca/P=1.66 for stochiometric HA [3]. Additionally, bone material contains 3% structurally incorporated water in addition to adsorbed water [11].

1.4 Solid Materials

Several biomimetic ceramic materials are being researched for use in bone tissue scaffolds. Hydroxyapatite seems to be a logical choice due to its similarity to bone mineral, but due to its insolubility in water stochiometric HA is not resorbable unless it contains impurities like carbonate, structural defects, or is nano-scale in size [12]. Tricalcium phosphate is chemically similar to hydroxyapatite but is less thermodynamically stable and is therefore more soluble in water and bioresorbable.

β-TCP ($Ca_3(PO_4)_2$) in water undergoes a slow dissolution and a hydroxylation reaction leading to the precipitation as HA. The dissolution and re-precipitation rate of β-TCP is ideal for bone tissue engineering since it more closely matches the bone growth rate [13]. There is also evidence that suggests that in physiological conditions β-TCP dissolution occurs through a cell mediated resorption process [12]. In vivo

testing has shown that at 32 and 52 weeks after implantation, β-TCP based bone grafts actually have a higher percentage of bone material than grafts made from deproteinated bovine bone [14].

45S5 Bioglass is used in bone grafts since it bonds strongly to both hard and soft tissues. In vitro testing has shown that 45S5 Bioglass releases Si^{4+} and Ca^{2+} ions which up-regulate gene expression for osteocalcin in MC3T3-E1 subclone 4 osteoblasts which is known to correlate with high bone density [15].

Table 1.1. Bulk Mechanical Properties of Relevant Materials

Species	**Elastic Modulus (GPa)**	**Compression Strength unless noted (MPa)**	**Source**
Cortical Bone	17-25 (Longitudinal) 10-12 (Transverse)	180-200 (Longitudinal) 120-140 (Transverse)	[13]
Trabecular Bone	0.2-1.0(Longitudinal) 0.01-0.4(Transverse)	4-12	[13]
Hydroxyapatite	40-100	90-120	[13]
45S5 Bioglass	0.35	42 (Tensile)	[16]
β-TCP (dense)	82.6	459	[17]
30%BG/β-TCP (2%Gelatin Binder)	-	0.714 (1 day in PBS) 8.22 (28 days in PBS)	[1]
30%BG/β-TCP (2%Laponite Binder)	-	0.809 (1 day in PBS) 5.08 (28 days in PBS)	[1]

1.4.1 Tricalcium Phosphate

Tricalcium phosphate is a commonly used bioceramic with the chemical formula of $Ca_3(PO_4)_2$. There are two main crystalline phases that are either stable or metastable at room temperature: β and α phases. The β-phase has a rhombohedral

crystal unit cell and is stable up to 1125 °C. The α-phase has a monoclinic crystal unit cell, is metastable at room temperature, and stable above 1125 °C. There is a third crystalline phase, α', but it is only stable above 1430 °C. Amorphous TCP when heated to 650 °C can convert directly to α-TCP and/or β-TCP [3].

1.4.1.1 Solubility and Cement Formation

Tricalcium phosphate undergoes a dissolution and re-precipitation reaction in aqueous solutions. In acidic solutions with a pH below 4.2, brushite (dicalcium phosphate dihydrate) precipitates and in solutions with a pH above 4.2 a calcium deficient hydroxyapatite (CDHA) precipitates instead [18].

Brushite Formation [19]:

$$Ca_3(PO_4)_2 + Ca(H_2PO_4)_2 \cdot H_2O + 7H_2O \rightarrow 4CaHPO_4 \cdot 2H_2O \tag{1.1}$$

Apatite Formation [19]:

$$3Ca_3(PO_4)_2 + H_2O \rightarrow Ca_9(HPO_4)(PO_4)_5OH \tag{1.2}$$

The ionic dissolution is governed by the Gibb's Free Energy Equation where: $\Delta_s G^0 = -RTln(K_{SP})$ and K_{SP} is the solubility product. The α-phase is more soluble than the β-phase, and HA is practically insoluble (Table 1.2).

Table 1.2. Solubility Products at 25°C [3]

Species	K_s
α-TCP	8.46×10^{-32}
β-TCP	2.07×10^{-33}
HA	6.62×10^{-126}

This lower solubility of β-TCP affects the reaction kinetics of cement setting/apatite formation due to the slower dissolution rate. It has been shown that in a 1 mol/L ammonia solution at 200°C, β-TCP takes 240 hours to convert to HA, while total conversion of α-TCP occurs in only 3 hours [20]. Another study showed that α-TCP cement set using a 2.5% Na_2HPO_4 solution and soaked in Ringer's solution had 78% conversion to CDHA and a compression strength of 32.7 MPa in 24 hours and 100% conversion to CDHA and a strength of 37.9 MPa in 360 hrs (15 days) [21]. For this reason, most research for injectable apatite type cements use α-TCP.

A study by Gbureck showed that converting β-TCP to an amorphous phase by high energy ball milling increases the reaction rate during a soak in a 2.5 wt % Na_2HPO_4 solution for 24 hours. The β-TCP (85.8% relative crystallinity) had only a 19.2% conversion into HA and a compression strength of 7.4 MPa, while amorphous-TCP (26.3% relative crystallinity) had a 92.7% conversion into HA and a strength of 51.0 MPa [22].

1.4.2 Bioglass

45S5 Bioglass is an older synthetic bioactive material developed in 1969 by Larry Hench in an effort to help regenerate bone for wounded Vietnam War veterans. During the initial in vivo animal testing, the surgeon performing the autopsies was unable to physically remove the Bioglass from bone at the implanted sites due to the strong bonding [23]. The FDA approved 45S5 Bioglass to replace the ossicular bone in the middle ear in 1985 and for orthopedic bone grafts in non-load bearing sites in 2000 [23]. For dental applications, 45S5 Bioglass is used under the trade names of Perioglass and Novabone to aide in bone grafting and under the trade name of Novamin as a toothpaste additive to treat dentin sensitivity.

45S5 Bioglass is a near eutectic soda-lime phosphosilicate glass mixture composed of the following: $45wt.\%SiO_2$, $24.5wt.\%CaO$, $24.5wt.\%Na_2O$, and $6wt.\%P_2O_5$. The high bioactivity of 45S5 Bioglass is due to the surface chemistry when exposed to water in physiological environments. The first reaction is a dissolution of Ca^{2+} and Na^+ ions and replacement with H^+ leading to the formation of $Si-OH$ bonds. An amorphous calcium phosphate layer is formed and the $Si-OH$ functional groups act as a nucleation source for the crystallization of a hydroxyl-carbonate apatite surface layer [16].

Studies have shown that during dissolution in biological conditions the Na^+ ion concentration range from 2937.0 to 4983.8 ppm, while the next highest concentration of ionic dissolution product is Ca^{2+} which only ranges from 47.5 to 88.3 ppm [24].

The dissolution of the Na^+ ions into the solution is a major issue during robocasting since it changes the zeta potential of the 45S5 Bioglass particles and destabilizes the suspension of Bioglass particles in the slurry which has led to some researchers using a dispersant in the slurry [25][26].

45S5 Bioglass is typically amorphous, but crystallization occurs at 677°C, and the glass transition temperature is 538°C [16]. There are concerns that full crystallization of 45S5 Bioglass renders the material bioinert instead of bioactive. There is some evidence that cell proliferation on partially crystallized Bioglass may be made comparable to the amorphous state with post-sintering treatments to functionalize the surface [27].

1.5 Binder Materials

1.5.1 Gelatin

Gelatin is derived from collagen by processing it with either strong acids or bases which hydrolyze the protein. Gelatin solutions form a gel by physically crosslinking when the solution cools below 35°C. This process is thermoreversible unless the solution is heated past 70°C [28]. The harsh processing conditions make gelatin less immunogenic than collagen and its biosafety has led to the use of gelatin in variety of regulated medical products [29]. Gelatin also has excellent biological properties supporting cell attachment, proliferation, and stem cell differentiation while being available at a low cost [30].

Gelatin sources are primarily bovine skins, pork skins, or bovine and pork bones, but processing gelatin from fish parts is a current research area since the different protein composition yields different properties and the process utilizes agricultural waste [31]. Mammalian sources tend to have a higher gel strength that fish. Due to the variation in the biological source material, gelatin is graded by its strength based on its resistance to penetration using an industry standard called the Bloom test [32].

1.5.2 Laponite

Laponite is a synthetic smectic clay nanoparticle used in several industries as a rheology additive due to its thixotropic (shear thinning) properties. It also has been used to create biocompatible hydrogels by physical crosslinking [33]. The chemical formula is:

$$Na^{+}_{0.7}[(Si_8Mg_{5.5}Li_{0.3})O_{20(OH)_4}]^{-0.7}$$

Laponite solutions are also sensitive to preparation conditions and can form several different age dependent sol, gel, colloidal, and glass phases which causes difficulty

when comparing results between different scientific studies [34][35]. The nanoparticles are disk shape and have a negative surface charge which causes the particles to form either a "house of cards" or "parallel partial overlap" stacking arrangement in a solution creating a glass or gel network [35]. The electrostatic interactions make laponite sensitive to ionic species in the solution (i.e. preparation in deionized vs tap water). The different phases are easily decomposed by the application of mechanical shear forces to the solution.

1.5.3 Oleic Acid

Oleic acid is a monounsaturated fatty acid common in vegetable and plant based oils. Olive oil is composed of 70% of oleic acid. The chemical formula is: $C_{18}H_{34}O_2$. The density is 0.887 g/cm^3 at 25°C.

Intravenous injection of oleic acid is known to cause acute pulmonary edema in certain mammals [36]. The median lethal dose (LD50) for oral consumption in rats is extremely high at 74,000 mg/kg, but the intravenous LD50 is only 2.4 mg/kg. For mice which don't suffer from the issues with pulmonary edema from oleic acid, the intravenous LD50 is 10 times higher at 230 mg/kg [37]. In this study, oleic acid was used a surfactant for the laponite binder to aid in robocasting. At concentrations of 2% by volume in the laponite binder and a powder/liquid ratio of two, 8.87 mg of oleic acid should be present per gram of base powder used (See Section 2.2.3). The oleic acid should be burned off in the sintering process, but for unsintered mixtures the concentration could be significant for certain animals.

CHAPTER 2

Research Methodology and Material Preparation

2.1 Objectives and Methodology of Current Research

The main focus of the current research is to improve the processing methods and mechanical strength of the scaffolds. While the material experiences significant strengthening after a long duration soak in PBS, the unsintered samples have a very low initial strength which makes them unsuitable for implantation. Sintering was performed at 500°C to increase the initial strength. Changes in the porosity, microstructure, and compression strength are evaluated in Chapter 3. Changes to the chemical structure were evaluated using X-ray Near Edge Absorption Spectroscopy (XANES) and discussed in Chapter 4.

Additive manufacturing has great potential for tissue engineering applications, but our initial processes for material preparation and robocasting suffered from poor repeatability. This made it difficult to reliably make scaffolds or to optimize the process. Robocasting is sensitive to the rheology of the slurry, and its repeatability was greatly improved with a more controlled process for binder preparation which is listed in Section 2.2.2. Robocasting is a deceptively simple looking process, and due to issues with repeatability the topic is presented as an engineering case study in Chapter 5.

The resolution of the robocasted scaffold is also a major limitation. The smallest raster width is restricted by the smallest usable syringe tip size which is 650μm for the mixtures. The ideal pore size for bone tissue scaffold is 100-150 μm. Since the minimum raster width is much larger than the target pore size, the scaffolds have

a low macro-porosity which limits the volume for which cells can infiltrate into the scaffolds therefore the biological functionality is reduced. The minimum tip size is related to the rheology of the slurry and the chemical dissolution and setting process when exposed to water. This behavior is fundamental to the slurry mixtures, so the use of non-aqueous binders and alternative silica sources was briefly explored.

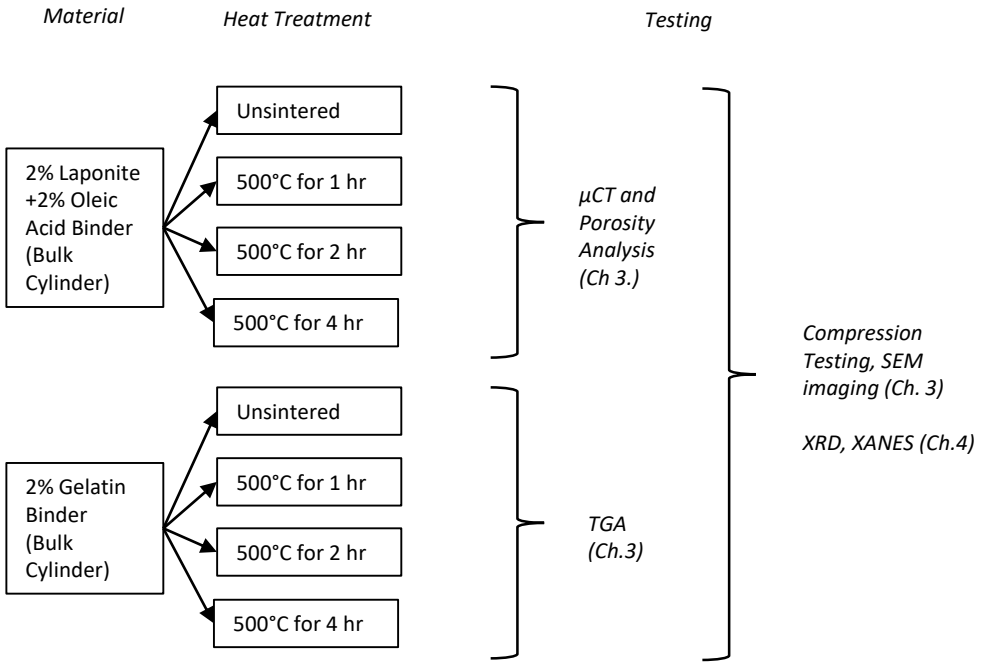

Figure 2.1: Experimental Setup for Bulk Samples

2.2 Materials Preparation

2.2.1 Ball Milling and Powder Preparation

β-TCP was purchased from Sigma-Aldrich. The 45S5 Bioglass was acquired from US Biomaterials (now Novabone Products) with a particle size of less than 90 μm. In order to mix the two powders and reduce the particle size, the 45S5 Bioglass

and β-TCP powders were ball milled for 24 hours unless otherwise specified. The grinding media used was yttria stabilized zirconia balls with a 5 mm diameter. Contact with water was avoided to minimize chemical reactions, so ethanol was used as a liquid phase. Before milling, the zirconia balls were dried at 110°C for approximately an hour to remove any adsorbed water. A low speed jar mill and 250 ml polyethylene bottle were used with the following amounts of material:

12g 45S5 Bioglass : 32g β-TCP : 40mL ethanol : 248g zirconia balls

After ball milling, the slurry was sifted into a petri dish and the remaining slurry was rinsed from the bottle and zirconia balls into the petri dish using ethanol. The slurry was dried at 60 °C for 2 hours and the dried cake of powder was then ground with an agate mortar and pestle.

The 45S5 Bioglass had an initial average particle size of 90μm as specified by the supplier. The 24 hr ball milling time was chosen since previous research determined it was sufficient for robocasting and SEM measurements which determined the final size of the powders to be 2.43 μm (std dev =0.62 μm) for the β-TCP and 30.23 μm (std dev =12.67 μm) for the 45S5 Bioglass [1].

2.2.2 Binder Preparation

Gelatin powder was added to de-ionized water at a 2% mass/volume ratio. The solution was mixed, allowed to hydrate for 1 to 3 hours, heated to 61°C, tempered at room temperature for 15 minutes, and then refrigerated a minimum of 16 hrs following the protocol for the standard Bloom test [32]. The gelatin solution was heated to 22±1°C immediately before use to reduce the viscosity and provide a consistent rheology of the slurry.

Laponite powder was added to de-ionized water at a 2% mass/volume ratio and mixed vigorously with a magnetic stirrer. The total mixing time was twice the time

required for the solution to clarify during the mixing process (approximately 10-15 minutes total). 90% oleic acid was added to the solution at a 2% volume/volume ratio to act as a surfactant and improve the printability of the slurry. Over time the oleic acid causes a precipitate to form from the solution, so oleic acid was only added to the solution on the day of use. Immediately before use, the solution was mixed vigorously with a magnetic stirrer to disperse gel phases to reduce age-dependent effects.

2% mass/volume ratios were used for the binders since the biological properties were already investigated in previous research [1]. For the gelatin binder, there are concerns that increasing the amount could cause issues with the burnout of organic molecules during sintering. At the beginning of the experiments, there were concerns that increased amounts of laponite may pose problems biologically due to the higher concentrations of lithium. Recently there was an in vitro study published which shows hydrogels have good cytocompatibility with concentrations of 7% laponite [33].

2.2.3 Slurry Preparation for Robocasting

The final slurry mixtures were mixed with a spatula for several minutes by combining 30% BG + 70% β-TCP powder with either the 2% gelatin or the 2% laponite mixtures. Unless otherwise specified, for robocasting, all samples had a powder to liquid ratio of 2 g powder to 1 mL of binder (P/L=2.00). For bulk compression test samples only, the slurry mixtures used P/L=2.667 (See Section 2.2.4). During initial mixing of the powder and binder, there is a tendency for it to seem like the binder amount is insufficient to fully wet out the powder, but this disappears after a sufficient mixing time.

2.2.4 Bulk Sample Molding

The final slurry mixtures were mixed with a spatula for several minutes by combining 30% BG + 70% β-TCP powder with either the 2% gelatin or the 2% laponite mixtures. Bulk compression test samples have a tendency to crack during drying due to uneven drying and high shrinkage rates, so the powder-to-liquid ratio was increased to reduce cracking. Bulk compression test samples had a powder-to-liquid ratio of 8 g powder to 3 mL of binder (P/L=2.667) and additional ethanol was added as needed to allow temporary flow of the slurry. Unless otherwise noted, all other samples the slurry mixtures used P/L=2.0 (See Section 2.2.3).

The slurries were pressed into plastic molds in the shape of ∅6.35mm cylinders [∅0.250 in] to comply with the alternative geometry allowed in ASTM C1424 [38] (and in accordance with ASTM C773 [39]). The molds were prepared by coating the surfaces with a silicone lubricant to act as a release compound. Due to the difficulty of fabrication, limited machinability, and reduced amount of material required the simple cylinder was used instead of the more accurate dumbbell shaped test specimen.

Samples were dried at room temperature for 3 days in an enclosed container to slow the evaporation rate in order to reduce drying cracks. Then samples were removed from the enclosed container and allowed to fully dry in ambient conditions for 4 days. The drying process was verified through use of a reference mold with several of the ∅6.35mm holes filled with water and the samples were assumed to be dry once all the water had fully evaporated from the reference mold. Once the room temperature drying process was complete, the samples were removed from the molds and heated at 60°C for 4 hours to help remove residual moisture before sintering.

Sintered samples were sintered per Section 2.2.5. After sintering, the tops and bottoms of the cylinders were ground down using a machine grinder to a height of

12.7mm [0.500 in] to comply with ASTM C1424. The circular side of the samples was left in the as-sintered condition due to the limited machinability of the material.

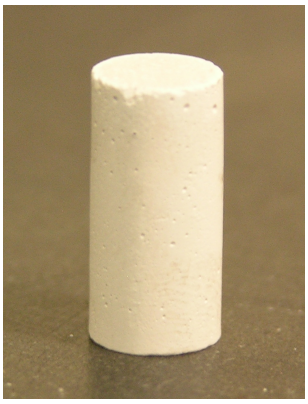

Figure 2.2: ∅6.35 x 12.7 mm tall bulk sample-gelatin binder, sintered 4 hr at 500°C, sides are as sintered, ends are ground flat

2.2.5 Sintering Process

Samples were sintered in a Thermolyne 6000 muffler furnace (ThermoFisher Scientific, Asheville, NC). The heating rate was 2℃ per min up to 500 ℃ and held for a specified amount of time (dwell time). The sinter dwell times for the bulk compression test samples were 1, 2, and 4 hours. At the end of the dwell time the oven was turned off and allowed to cool to for approximately 17 hours.

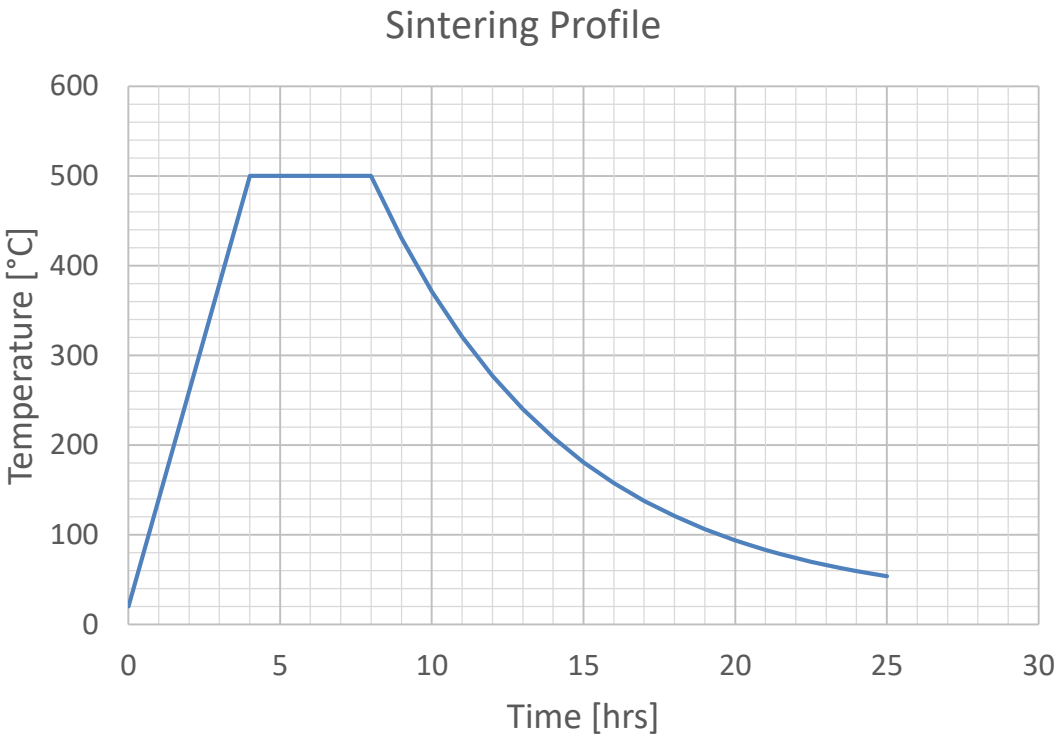

Figure 2.3: Sintering profile for a 4 hr dwell time

CHAPTER 3

Sintering Characterization

3.1 Introduction

Due to the high melting temperatures and limited ductility of ceramics, it is typically impractical to fully melt and cast a ceramic part as a manufacturing process. The common alternative is to sinter the ceramic material, where the ceramic is ground into a fine powder to raise its surface energy, the powder is formed into a net shape called a green body. The green body is then heated to a temperature below its melting point where diffusion moves material to bond together the separate powder grains to reduce the size of interfaces and thereby lower the surface energy. A major issue with powder processing, and hence sintering, is that it inherently introduces pores into the material [40]. Therefore, to improve the mechanical properties of a material, it is important for a sintering process to increase a ceramic material's density.

As discussed previously (Section 1.1.4.2) crystallization of 45S5 Bioglass negatively impacts its biological properties. The need to prevent BG crystallization is a major limitation on the allowed sintering temperatures for the 30% BG + 70% β-TCP mixtures. A sintering temperature of 500°C was chosen since previous research showed that the mixtures had significant crystallization of the 45S5 Bioglass when heated to 700°C, but not when heated at 500°C [1]. The low sintering temperature was expected to cause a small but modest increase in compression strength.

There is evidence that Bioglass acts as a sintering aid for β-TCP at higher temperatures. One study by Bergmann co-sintered a mixture of 60% Bioglass + 40% β-TCP at 1000°C, which is above the crystallization temperature of Bioglass but

below the transition temperature from β-TCP to α-TCP [41]. Analysis of the resulting material revealed only $NaCaPO_4$ and $CaSiO_3$ phases present in the mixture. Another study by Lopes, co-sintered a 7.5% Bioglass + 92.5% β-TCP mixture at 1200°C [42]. In the resulting material, α-TCP and β-TCP phases were present, but no crystallized Bioglass which seems to indicate that the Bioglass was incorporated structurally into the TCP crystal structure.

Bulk compression test sample geometries were chosen for mechanical testing instead of robocasted/AM samples since currently there is no standard AM test geometry for this class of materials. Also, in the robocasted scaffolds there are effects from interlayer bonding, geometric effects, and process variations which would be difficult to quantify without a comparison to bulk sample compression test data. Individual extruded rasters could be tested in a 3 or 4 point bend tests, but there would be issues with the test setup due to the small geometries and loads involved.

Thermogravimetric analysis was performed to help characterize the heating cycle and verify that there is no significant mass loss at the sintering temperatures. A study showed that the weight of 45S5 Bioglass reduces to 93.6% at 700°C, but when the NaO content was replaced with CaO the weight change was less than 1% [43].

3.2 Material and Methods

Cylindrical bulk compression test samples were fabricated per Section 2.2.2.4 (P/L=2.667) using either gelatin or laponite binders and were sintered per Section 2.2.2.5.

3.2.1 Thermogravimetric Analysis (TGA)

Samples were prepared for TGA testing per Section 2.2.2.3 (P/L=2.0) and the slurry was allowed to fully dry at room temperature before testing. Approximately

20 mg samples were used for testing with a sample size of 3. A Pelkins-Elmer TGA7 machine was used with N_2 as a purge gas at a flow rate of 30 mL/min. The samples were heated at a rate of 5°C per min up to 700 °C.

3.2.2 X-ray Computed Tomography

Bulk compression cylindrical compression test samples were scanned for only the laponite binder samples. Due to limited machine access, a total of only 4 samples were scanned (2 separate scans with 2 samples each) at a sample size of 1 for each heat treatment.

The scans were performed on a X5000 X-ray CT system (North Star Imaging, Rogers, Minnesota) with the beam operating at 70 kV and 335 mA and the camera shooting at 2.5 frames per second. The image resolution was 5.26 μm per voxel (24.17X Magnification). Scan processing was performed using North Star Imaging software and image slices of the CT scan volume were exported for analysis with a 5.26 μm spacing between slices. Voids are clearly differentiated by the image density contrast due to the large difference in density (3 orders of magnitude).

Image analysis was performed using ImageJ processing software (`https://imagej.nih.gov/ij/`). The porosity was determined by measuring the area percentage of voids in a 10 mm^2 section in the center of the sample over a set of image slices along a defined sample length. The samples were scanned before grinding and the top ends had a large number of cracks that would later be removed, therefore the very top of the scanned volume was not used in the porosity analysis. There is a large variability in the porosity of the sample due to manufacturing defects, so the porosity analysis was also re-tabulated to contain data from the bottom 2.63 mm (500 images) of the scan volume in an effort to get a more representative selection of data.

3.2.3 Mechanical Compression Testing

Compression testing was performed per ASTM C1424 on an Instron 5567 Universal Testing System using displacement control at an applied strain rate of 1.3 mm/min [38]. A 35 N preload correction was used to account for slack in the Instron test machine. The test was either stopped automatically when the rate of change in the load measurement exceeded 40% or stopped manually when the sample began to experience sequential failures which did not exceed the 40% rate of change.

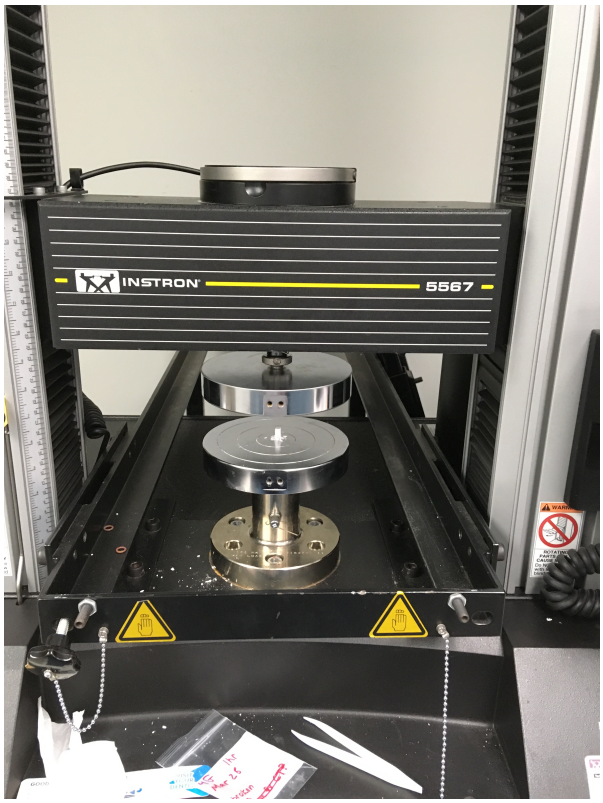

Figure 3.1: Compression test machine setup

3.2.4 SEM Imaging

After compression testing, the samples were sputtered with carbon for 5 minutes using a CrC-100 Sputtering System operating with argon plasma at 8 millitorr of

pressure. The fracture surface of the samples were imaged with a Hitachi S-3000N Variable Pressure SEM operating at a high vacuum and using an electron beam voltage of 25 kV using the Secondary Electron Imaging mode (SEI).

3.3 Results

3.3.1 Thermogravimetric Analysis (TGA)

At 700°C, average sample mass reduced to 95.38% (4.62% reduction) for gelatin samples (Fig 3.2). At the sintering temperature of 500°C, the average mass reduced to 95.75%. A total weight loss of 1.32% occurred as the samples were heated up to 100°C which is indicative of water loss, but the majority of the weight loss, 2.10% reduction, occurred between 200 and 400°C.

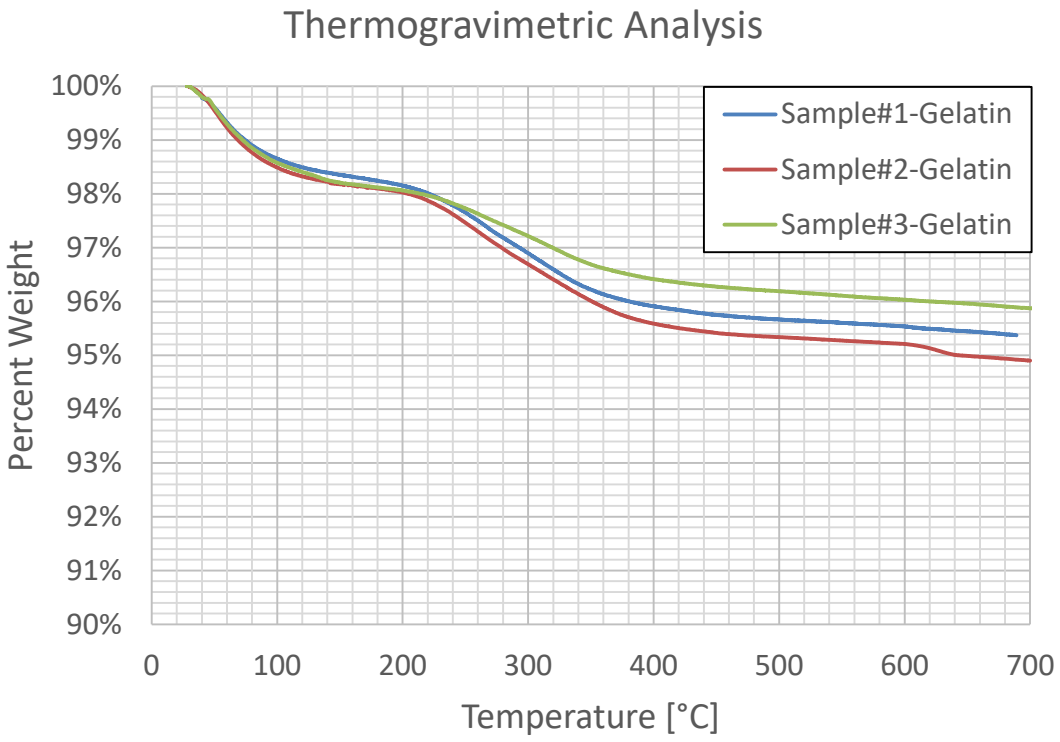

Figure 3.2: TGA of dried mixture with 2% gelatin binder

The TGA data corresponds well with existing literature. The general curve shape is similar to a 2012 study by Zhang on electrospun gelatin-β-TCP nanoparticle mixtures with the β-TCP content ranging from 0-20% [44]. The study by Zhang showed significant weight loss due to the large gelatin content, but had similar changes in slope near 100, 250, and 325°C.

3.3.2 CT Scan/Porosity Changes

CT scans show that the samples have high micro-porosity (Fig. 3.3) with large voids, cracks, and inclusions in all of them (Fig. 3.4). The presence of large voids skews the overall porosity measurements which is evident in the large difference in porosity along the length of the sample. For example, in the 2hr sample the porosity changes from 50.0% to 71.9% within only a 1.2 mm section of the sample (Fig. 3.6 from z=6.1 to 7.3mm). Porosity data was analyzed for both the majority of the sample length and from the bottom 500 slices of the CT scan (2.63 mm) in an effort to get more representative data, but for the 4 hr sample this bottom section of the sample length contained areas of high porosity (Fig. 3.5).

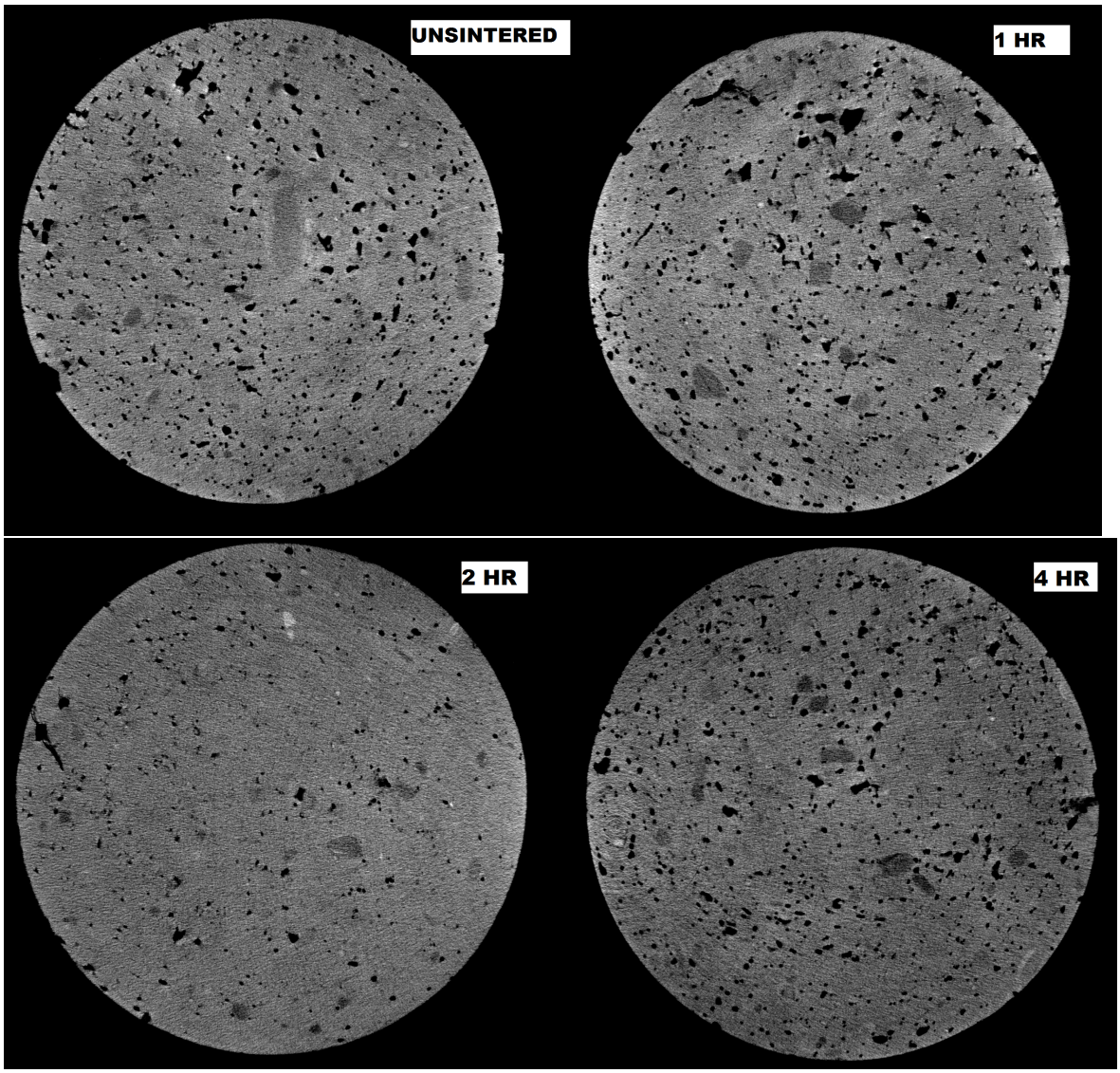

Figure 3.3: CT scan image cross section of laponite binder samples for unsintered and 1, 2, and 4 hr sinter dwell times

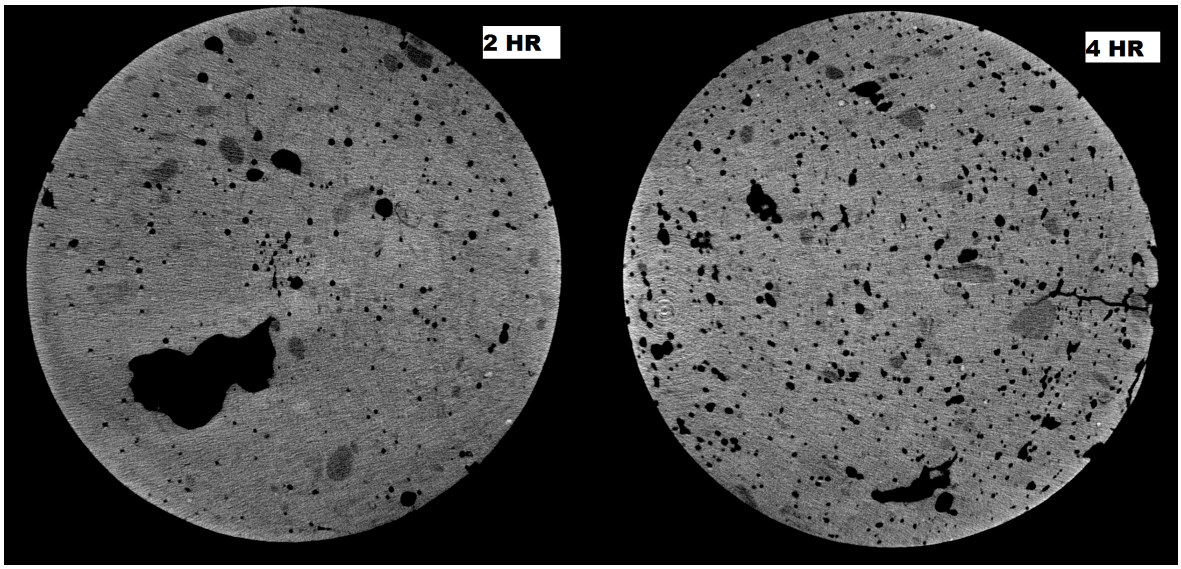

Figure 3.4: CT scan image cross section showing large voids and cracks for the 2 and 4 hr sinter dwell times

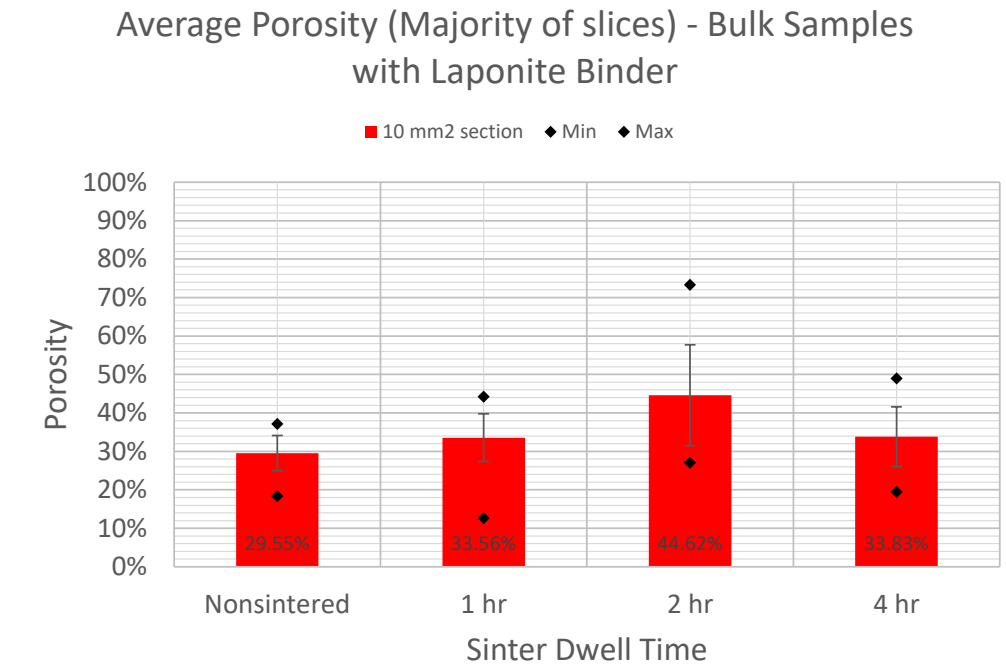

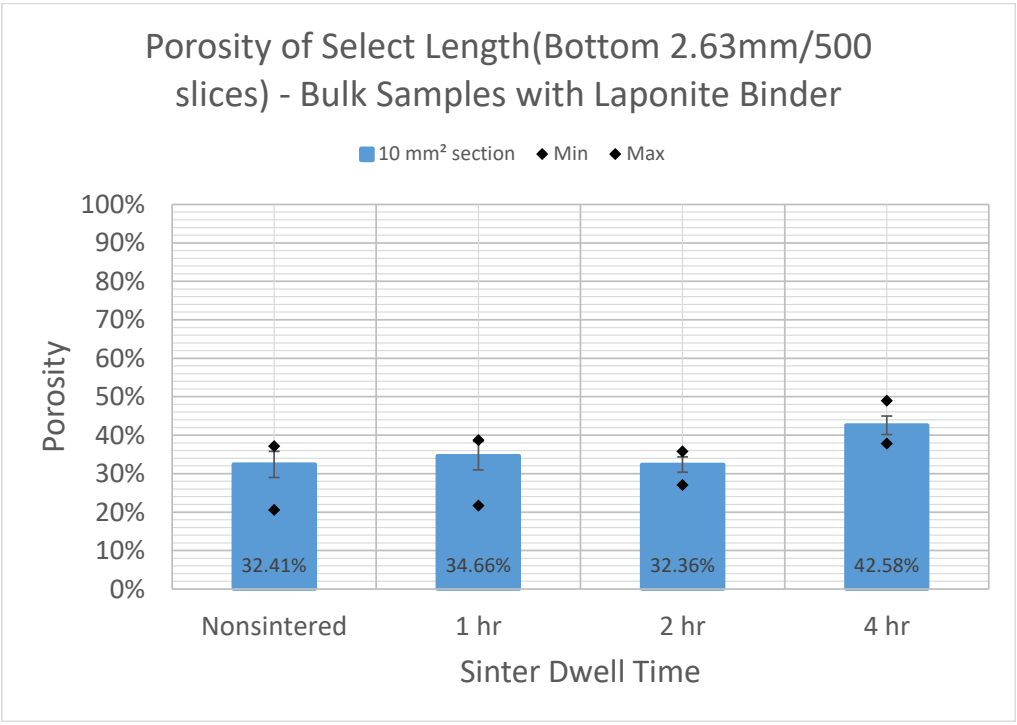

Figure 3.5: Porosity Measurements along given sample length

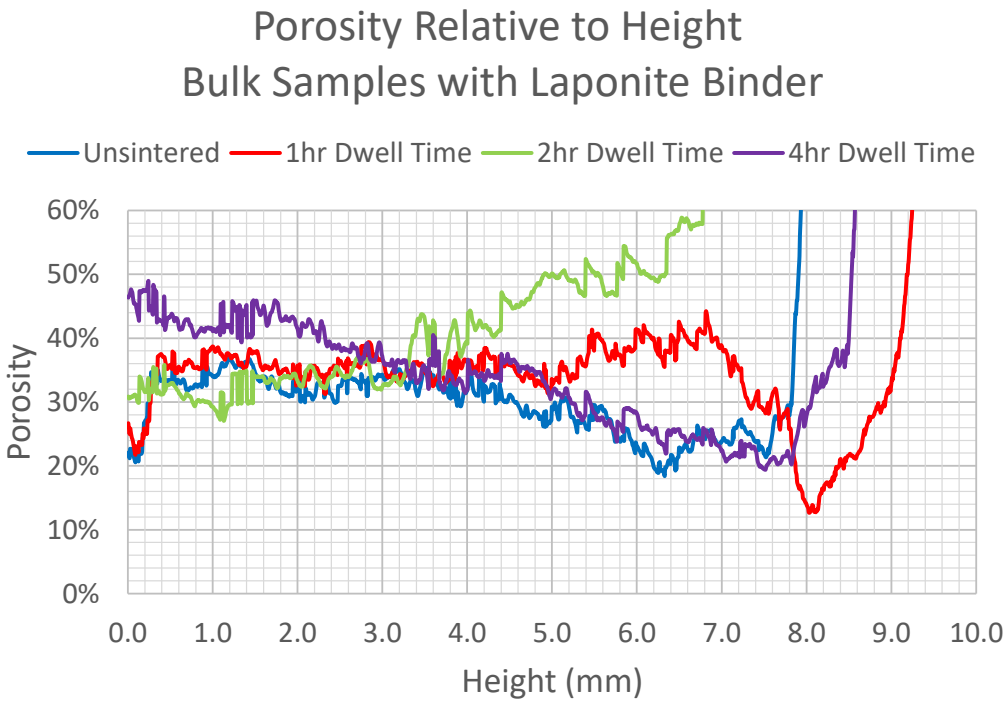

Figure 3.6: Porosity Measurement versus sample length

Table 3.1. Porosity and Strength of Individual Samples

Sinter Dwell Time (hrs)	Porosity of Majority of Sample	Porosity of Bottom Section	Tested Compression Strength (MPa)
Unsintered	29.55%	32.41%	6.79
1	33.56%	34.66%	8.48
2	47.28%	32.36%	7.85
4	33.83%	42.85%	10.71
Average	36.06%	35.50%	8.46

3.3.3 Compression Strength

The gelatin binder samples did not show any significant increase in strength with longer sintering times, but the laponite binder samples showed a roughly linear increase in strength (Fig. 3.7). The average elastic modulus was 1.31 GPa for the gelatin binder samples and 1.33 GPa for the laponite binder samples. The samples failed either by simple crack formation or by progressive failures as sections of the sample flaked off (Fig. 3.8).

Although the compression strength of the laponite binder samples responded more strongly to sintering, qualitatively the gelatin samples appear to have a higher green body strength. This is evident from the large number of laponite samples that were damaged during fabrication, typically during the grinding (Table 3.2).

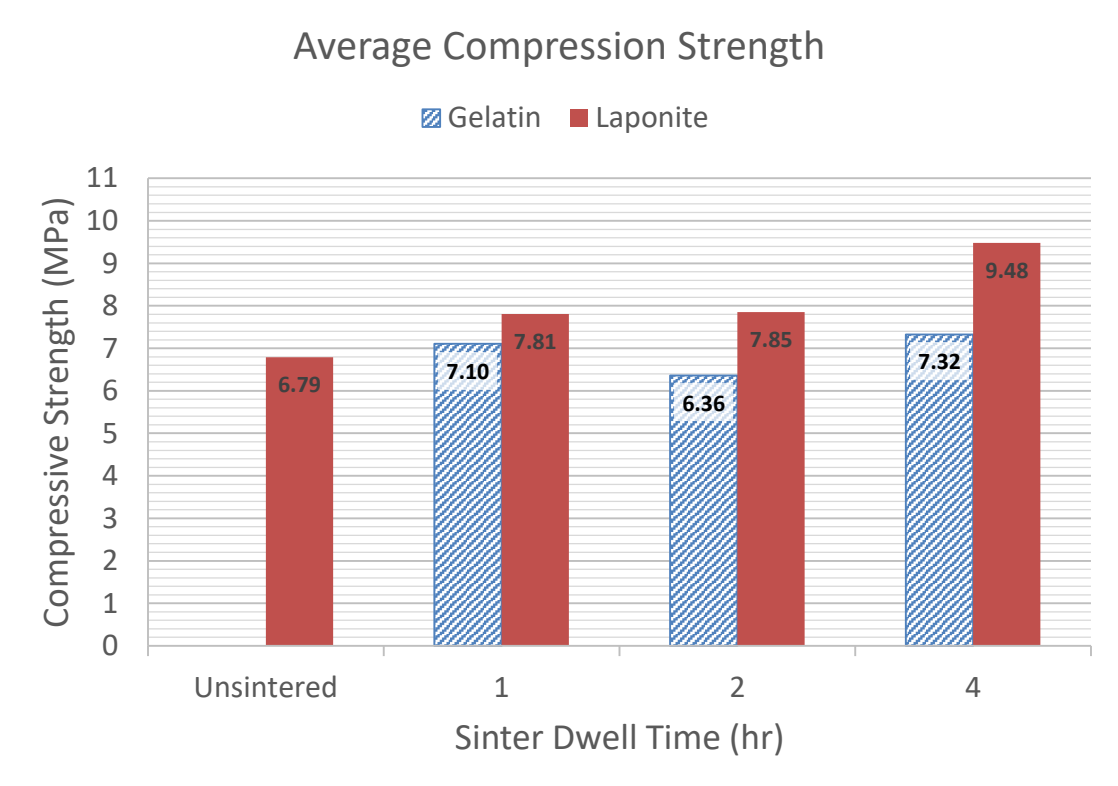

Figure 3.7: Compression Test for Sinter Times of 1, 2, and 4 hr at 500°C

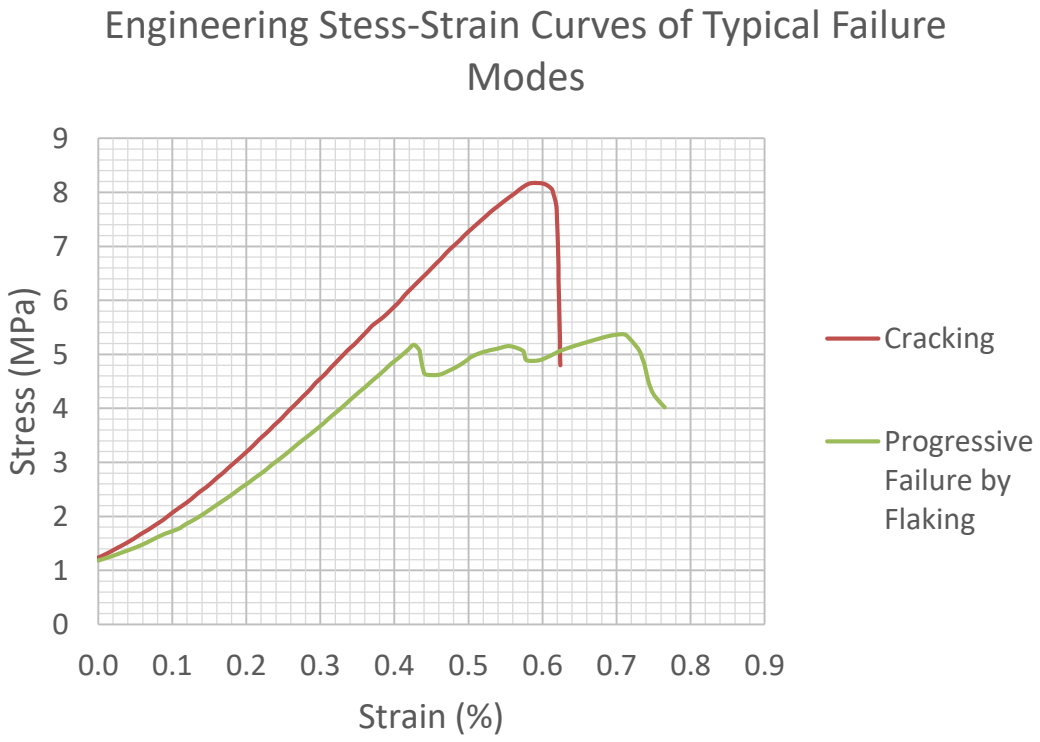

Figure 3.8: Engineering stress-strain curve showing the typical failure modes. The examples are gelatin binder samples with a 1 hr sinter dwell time

Table 3.2. Sample number for tests performed and fabrication process survival rates from green body stage to compression testing

Sinter Swell Time	Gelatin Binder		Laponite Binder	
	Final Sample Size	Survival Rate	Final Sample Size	Survival Rate
Unsintered	-	-	1	25%
1 hr	3	75%	4	100%
2 hr	3	100%	1	25%
4 hr	3	80%	2	50%
All		92%		50%

3.3.4 SEM Imaging

SEM imaging shows relatively smooth fracture surfaces which is indicative of brittle failure and transgranular cracking which was expected (Fig. 3.9). Fig 3.10 shows sharp edges on the individual sintered grains which indicates that significant surface diffusion didn't occur during the sintering process.

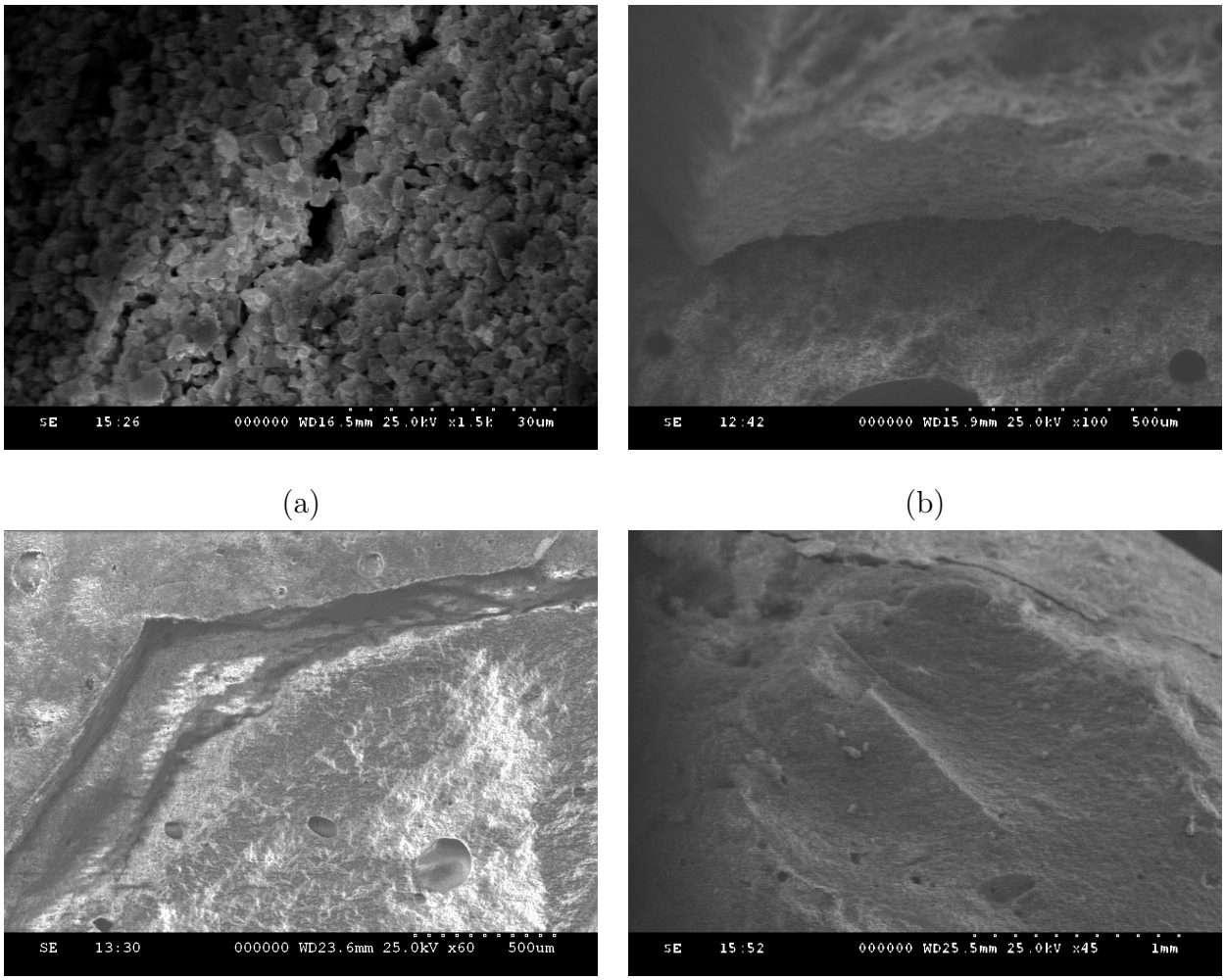

(a) (b)

(c) (d)

Figure 3.9: SEM Images of fracture surface (a) transgranular crack, (b), (c), and (d) fracture surface indicative of brittle failure

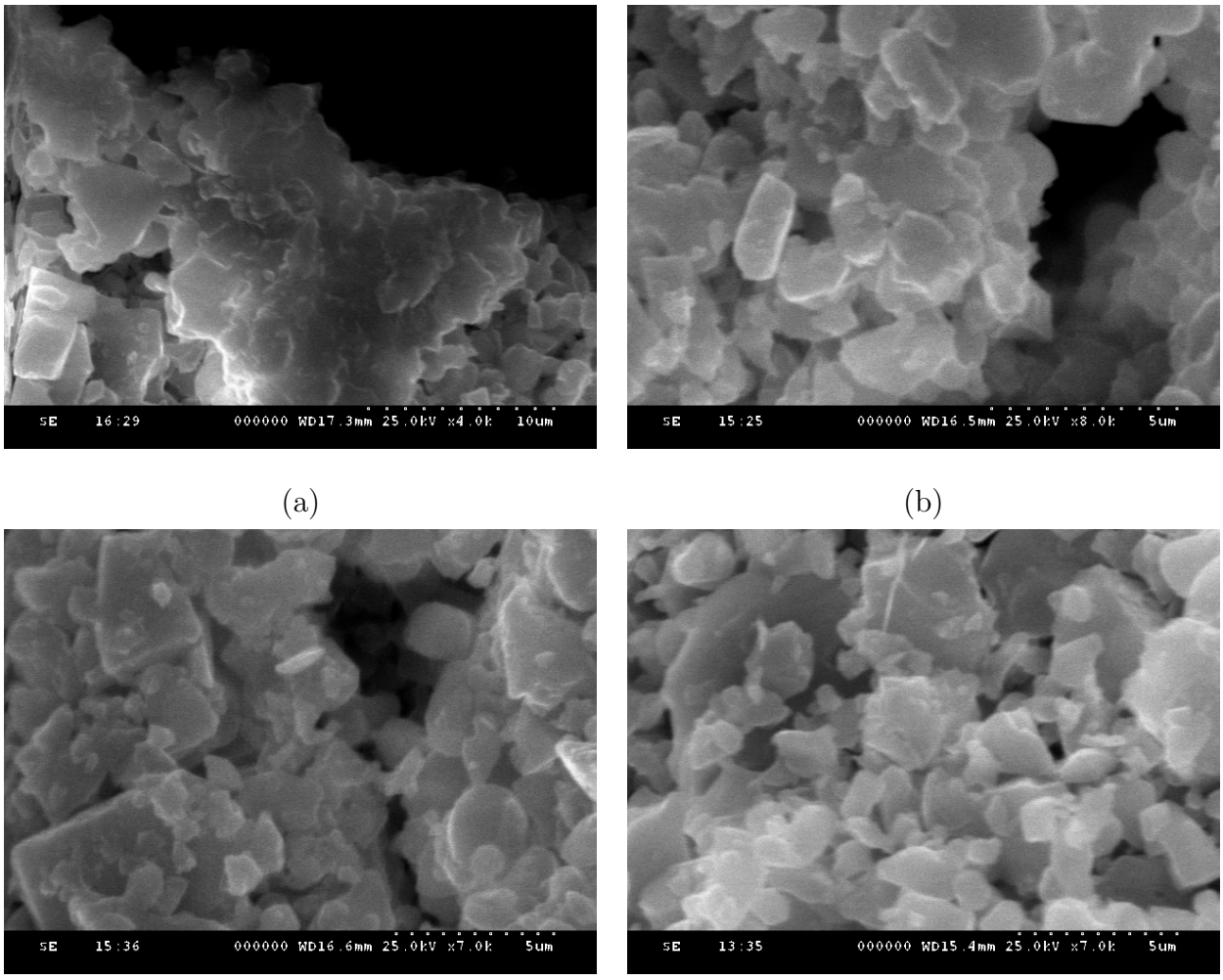

(a) (b)

(c) (d)

Figure 3.10: SEM images of microstructure of sintered samples showing particles in the 1 to 20 μm range

3.4 Discussion

Fabrication of the bulk samples was problematic due to the low green body strength of the samples which required a reduction in the amount of liquid binder and control of the humidity during the drying process as well. Also, the high viscosity of the slurry makes it difficult to completely fill the molds and likely contributed to

the high number of large voids in the samples. This creates a selection bias in the data since the weakest samples are destroyed during the sample fabrication process. While 92% of the gelatin binder samples survived the process, only 50% of the laponite binder samples (total) and 25% of the unsintered laponite binder samples survived. Robocasted scaffolds did not have apparent issues with drying cracks which is likely due to the high surface area and even drying, although issues may become evident after sintering. Using individual robocasted raster lines as the mechanical testing geometry may likely be less problematic due to the better drying characteristics.

The increased strength from the sintering process allowed for the tops and bottoms of the samples to be ground flatter and more parallel by using machining equipment, and this better geometric tolerance improves the accuracy of the compression test. This causes an issue when comparing the sintered strengths to the previous data from Chien-Ning Yao (Anabelle). The single unsintered laponite sample to survive the grinding process had a reported compression strength 5.9 MPa higher than similar samples from the previous PBS soak test (at soak time =1 day). With such a limited sample size in the current testing it is difficult to determine how much of the reported increase in strength is due to the sintering process and how much is from the edge grinding.

The sintering temperature of 500°C is relatively very low and was chosen to prevent crystallization of the 45S5 Bioglass. Sintering increased the compression strength of the samples, but the magnitude of the increase was low. Analysis of the CT scan data didn't show a significant decrease in porosity from sintering. SEM images of the microstructure also show sharp edges which indicates little diffusion occurred during the sintering. All this is indicative that a higher sintering temperature is needed.

3.5 Conclusion

While the samples with laponite binder responded the best to sintering, the increase in compression strength was small. No clear trend in densification occurred, and the microstructure shows sharp edges indicating that little diffusion occurred. At 500°C sintering occurs, but a higher sintering temperature is needed for the process to be an effective strengthening mechanism. Sintering temperatures in the range between 538°C (BG glass transition temperature) and 677°C (BG crystallization temperature) should be investigated. The exact effect that the composition of the 30% BG + 70% β-TCP powder mixture has on the Bioglass crystallization is unknown, so the absence of BG crystallization needs to be verified for any new higher temperature sintering processes.

CHAPTER 4

XANES Analysis

4.1 Introduction

4.1.1 XANES

X-ray absorption spectroscopy (XAS) uses the excitation of an atom's core electrons from their ground state to an excited state in order to capture information about the atomic electron shell structure and molecular orbitals in a material. XAS is sensitive to the local structure of an atom and is useful for determining the surface chemistry of both amorphous and crystalline samples.

The energy range of the spectra is determined by the element and the quantum number of the electron shell being probed (i.e. the K, L, and M edges). The spectra is divided into 2 ranges. The first part of the spectra is called X-ray Absorption Near-Edge Structure (XANES) or Near-Edge X-ray Absorption Fine Structure (NEXFAS). XANES contains information from multiple scattering events (forward and back scattering) and gives information on electron shell structure and symmetry. The next part of the spectra is called Extended X-ray Absorption Fine Structure (EXAFS). EXAFS contains information mainly from single scattering events and gives information on bond numbers, types, and distances to ligands and neighboring atoms [45][46].

XANES testing is performed using a synchrotron particle accelerator as a light source. Electrons are accelerated to relativistic speeds and when an electron decelerates due to a bend in the beam line they lose energy by emitting a photon. This creates an extremely brilliant, polarized, and collimated light over a wide range of

wavelengths in the UV to X-ray spectrum. A diffraction grating or other monochromator is then used to scan the sample along a select range of wavelengths.

4.1.2 Sample Composition

The initial powder mixture is 30%BG and 70%β-TCP by weight. The molar composition of the mixture is 72.16% oxygen, and the majority of the calcium and phosphorus are segregated in the β-TCP (Table 4.1 and 4.2).

Table 4.1. Molar Composition of Powder Mixture by Element

	Atomic Species				
	O	Na	Si	P	Ca
β-TCP	61.54%	0%	0%	15.38%	23.08%
45S5 Bioglass	82.26%	6.80%	6.45%	0.73%	3.76%
30%BG + 70%β-TCP	72.16%	3.49%	3.30%	7.88%	13.18%

Table 4.2. Source of Elements in 30% 45S5 Bioglass + 70% β-TCP Powder

	Atomic Species				
	O	Na	Si	P	Ca
β-TCP	41.59%	0%	0%	95.27%	85.39%
45S5 Bioglass	58.41%	100%	100%	4.73%	14.61%

For biologically relevant calcium phosphates, apatites often coexist as a mixture with precursor calcium phosphate compounds, and XANES is a useful tool for studying the materials [47]. XANES has been used in the study of biological apatites in bone [48][49][2] and has also been used to evaluate the sintering of hydroxyapatite

and 45S5 mixtures to determine the type of silicate and phosphate bonding preset [50].

Silicates are a broad and complex topic. The basic structural unit of silica is SiO_4^{4-} tetrahedra but it can form six different structural units including rings, chains, and sheets [40].

In the Na_2O–CaO–Al_2O_3–SiO_2 glass system, sodium disrupts the glass network by substituting for silicon atoms in the SiO_4 tetrahedra. The resulting oxygen bond types are called bridging oxygen (BO) for Si-O-Si bonds between SiO_4 tetrahedra and non-bridging oxygen (NBO) fo Si-O-Na bonds. This is clearly visible in XANES spectra due to the difference in binding energy between the BO and NBO bonds [51][52]. Instead of substituting for silicon, calcium forms a Ca-O polyhedra when it is incorporated in the glass network [53]. In this system, non-bridging oxygen atoms will preferentially bond with calcium instead of sodium [54].

4.2 Methods and Materials

Samples were prepared per Section 2.2.4 (P/L=2.667) and then were processed with 4 different sintering profiles per Section 2.2.5: unsintered, sintered at 500°C for 1, 2, and 4 hr dwell times. After compression testing per Section 3.2.3, the samples were ground into a powder using an agate mortar and pestle.

4.2.1 X-ray Diffraction

X-ray diffraction tests were performed to verify the composition of the samples and to check for the presence of HA formation prior to XANES testing. Powder samples were analyzed with a Siemens D-500 Powder Diffractometer using copper K_α X-ray radiation ($\lambda = 1.54\text{Å} = 8040$ eV) in a $\theta - 2\theta$ configuration. The acceleration

voltage was 40 kV and the current was 30 mA. 2θ values ranged from 10° to 65° with a step size of 0.1° and a 0.1 s dwell time per step.

4.2.2 XANES

Samples were analyzed along with β-TCP, 45S5 Bioglass, HA nanopowder, SiO_2 nanopowder, amorphous SiO_2 (glass slide), calcium silicate, sodium silicate, and powdered laponite as reference materials. The powder samples were mounted on carbon tape. The β-TCP used as a model compound has a minimum of 96% purity as stated by the manufacturer (Sigma-Aldrich, CAS Number 7758-87-4). The standard requirement for implantation is 95% pure β-TCP per ASTM F1088 [55].

XANES spectra were obtained using a sychrotron light source at the Canadian Light Source in Saskatoon, Canada. The silicon and phosphorus $L_{2,3}$-edge spectra were measured on the Variable Line Spacing Plane Grating Monochromator (PGM) beamline and the oxygen K-edge spectra was performed on the High Resolution Spherical Grating Monochromator (SGM) beamline. The step size was 0.10 eV with a 1.0 s dwell time. All data was normalized by dividing by the incident photon energy, I_0.

For silicon and phosphorus $L_{2,3}$-edge, fluorescence yield (FLY) measurements were used since the low electrical conductivity of the samples caused unacceptable levels of noise in the total energy yield (TEY) measurements. A baseline subtraction was used for the phosphorus data but not for silicon.

For the oxygen K-edge data, the TEY measurements were less noisy than the FY measurements so the TEY data was used. There appears to be a significant shift in peak positions from published data, so all oxygen K-edge data was shifted -3.95 eV, to match the β-TCP peak positions to a 2013 study by Rajendran [48].

4.3 Results and Discussion

4.3.1 X-ray Diffraction

X-ray diffraction results verified that the only crystalline phase present is β-TCP which was expected (Fig. 4.1). The 500℃ sintering temperature is too low to cause transformations into α-TCP or crystallize the Bioglass. The samples were mixed with a water based binder during fabrication, so there is some potential for HA formation by both the β-TCP and Bioglass, but there is no evidence of any significant amounts of crystalline HA phases present.

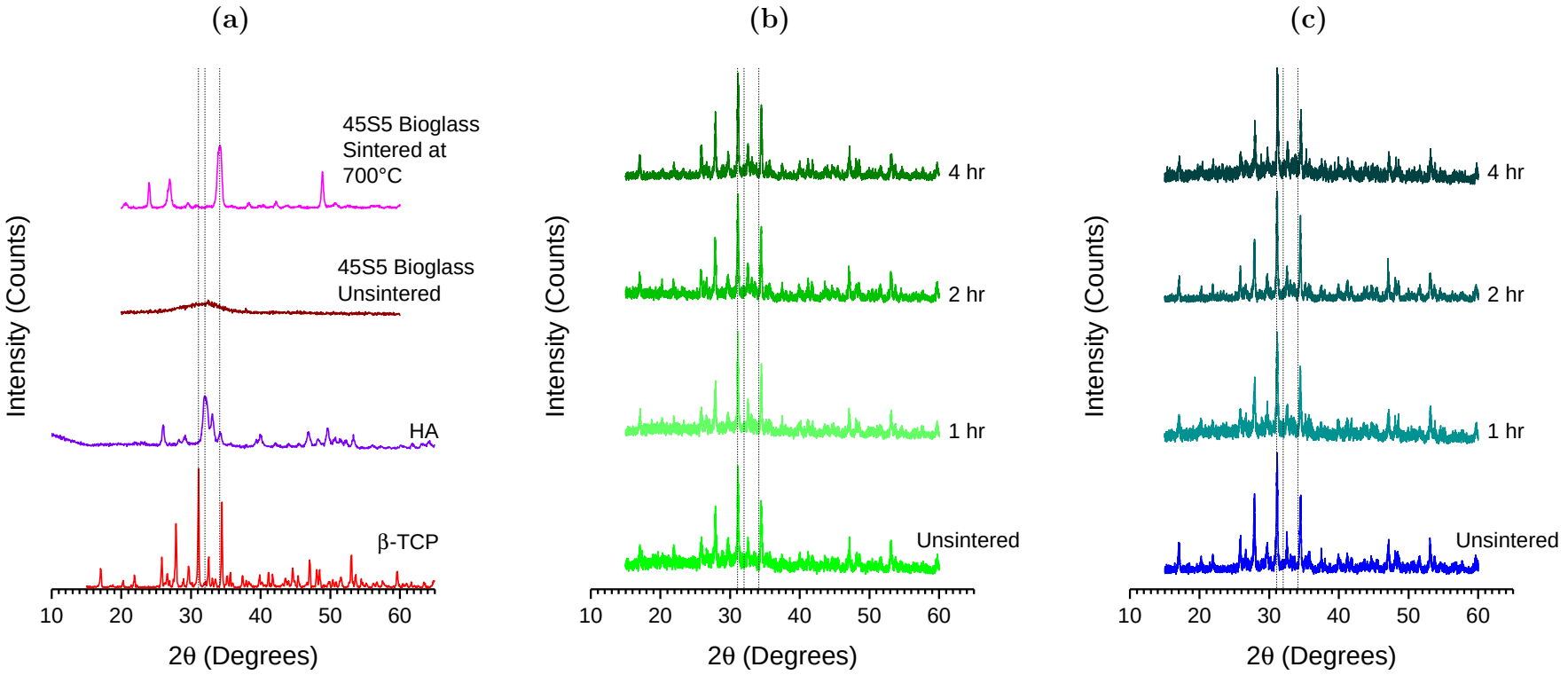

Figure 4.1: X-Ray diffraction data for (a) Model compounds (b) Gelatin binder samples (c) Laponite binder samples

4.3.2 XANES Silicon $L_{2,3}$-edge

Pre-edge peaks A and B are a doublet due to spin-orbit interactions of the 2p orbitals (Si 2p to Si 3s orbital transition) [50]. The sintering times of the samples changes the ratio of the A and B peak heights (Fig. 4.3). For the gelatin binder samples, there is no clear trend with changes in sintering time. For the laponite binder samples, there is a clear linear decrease in the ratio with longer sintering times which indicates that the laponite is active in the sintering process and aids in the sintering. The A/B peak height ratios are higher than all the samples but are closest to sodium silicate which indicates a similarity in Si bond types.

Calcium silicate has a distinguishing pre-edge peak D [50]. While there is a subtle change in the pre-edge near the peak D location in the laponite and gelatin binder samples, there is no clear peak which indicates that calcium is not being incorporated into the glass network. The majority of the calcium is in the β-TCP and appears to be too far away to influence the silicon bonds

Deconvolution of the main peak C was problematic with this data, due to the fact that the samples are a mixture. There are several small shifts in the main peak positions between the different model compounds. The samples require a smaller step size and a longer step dwell time to increase the resolution in order to properly resolve and deconvolute the peaks and determine the main contributions to bonding.

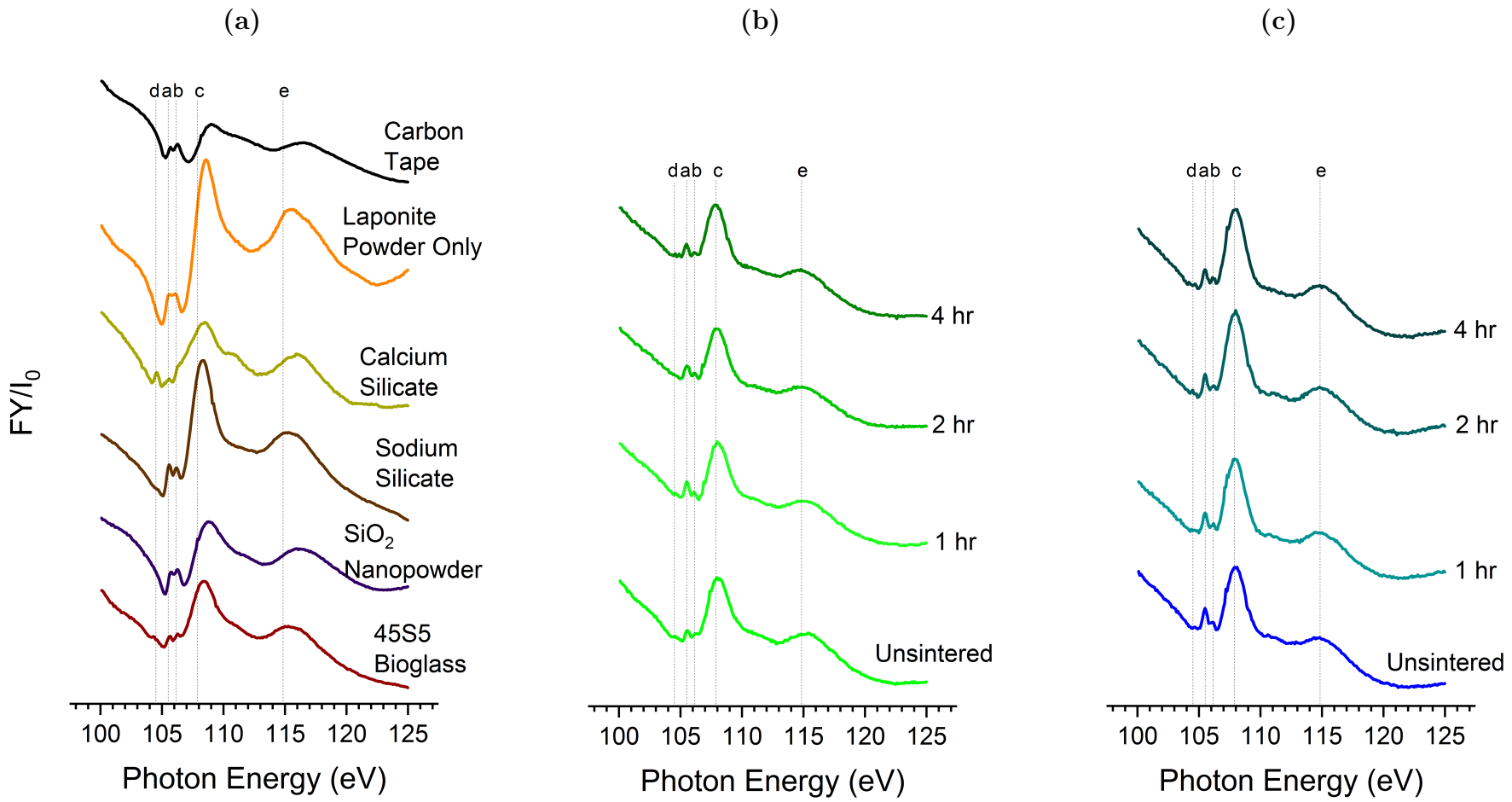

Figure 4.2: Silicon $L_{2,3}$-edge (a) Model Compounds (b) Gelatin Binder (c) Laponite Binder

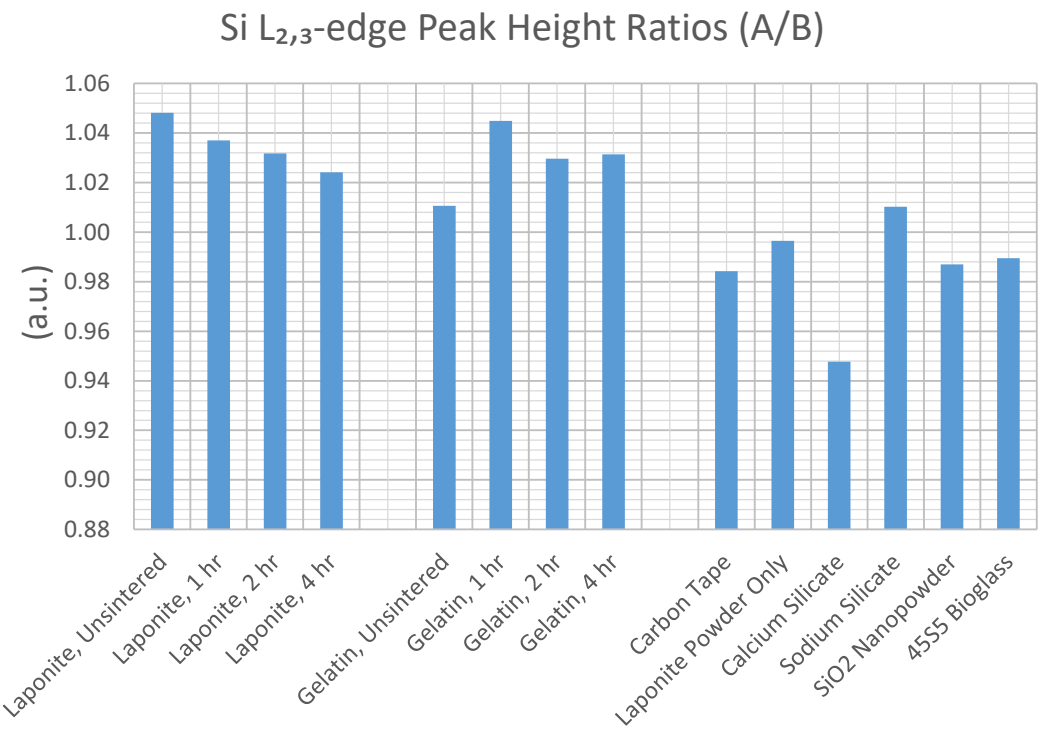

Figure 4.3: Ratio of A/B peak heights

4.3.3 XANES Phosphorus $L_{2,3}$-edge

The samples are more similar to HA nanopowder than β-TCP. Since the XRD data does not show the presence of crystalline HA, this is likely a thin amorphous surface layer of HA and not representative of the bulk composition of the material. The penetration depth of the lower energy X-rays used for the P $L_{2,3}$-edge should be in the range of a few tens of nanometers, while the higher energy X-rays used for the XRD should penetrate deeper into the sample.

There is little change in the sample peaks between the different sintering conditions which indicates that the phosphate, as expected, is not changing chemically since the majority of the phosphorus is in the β-TCP. The Bioglass signals are relatively noisy due to the small amounts of phosphate present.

Peak E is thought to be a 2p electron in phosphorus transitioning to an empty 3d shell in calcium [50]. Other studies show a much less prominent post-edge shoulder (peak E) in β-TCP model compounds(Fig 4.5) [50],[2],[48],[49]. The minimum purity of the β-TCP used in this study is 96% as listed by the manufacturer where the study by Rajendran used 99% pure β-TCP [48].

The height of the post-edge shoulder indicates an increase in the number of Ca atoms neighboring the P atoms, which means the Ca/P value is higher than the stochiometric value of Ca/P=1.5. The increase Ca/P ratio is likely due to the presence of tetracalcium phosphate, but this needs to be verified by further testing. On the $P_2O_5 - CaO$ phase diagrams, for calcium rich mixtures, β-TCP and tetracalcium phosphate should be present. Also tetracalcium phosphate (Ca/P=2.0) is the only calcium orthophosphate with a higher Ca/P ratio than apatites (Ca/P= 1.5 to 1.66). The XRD tests did not indicate the presence of tetracalcium phosphate, but XRD will only pick up crystallized phases and the XRD scan had a short dwell time.

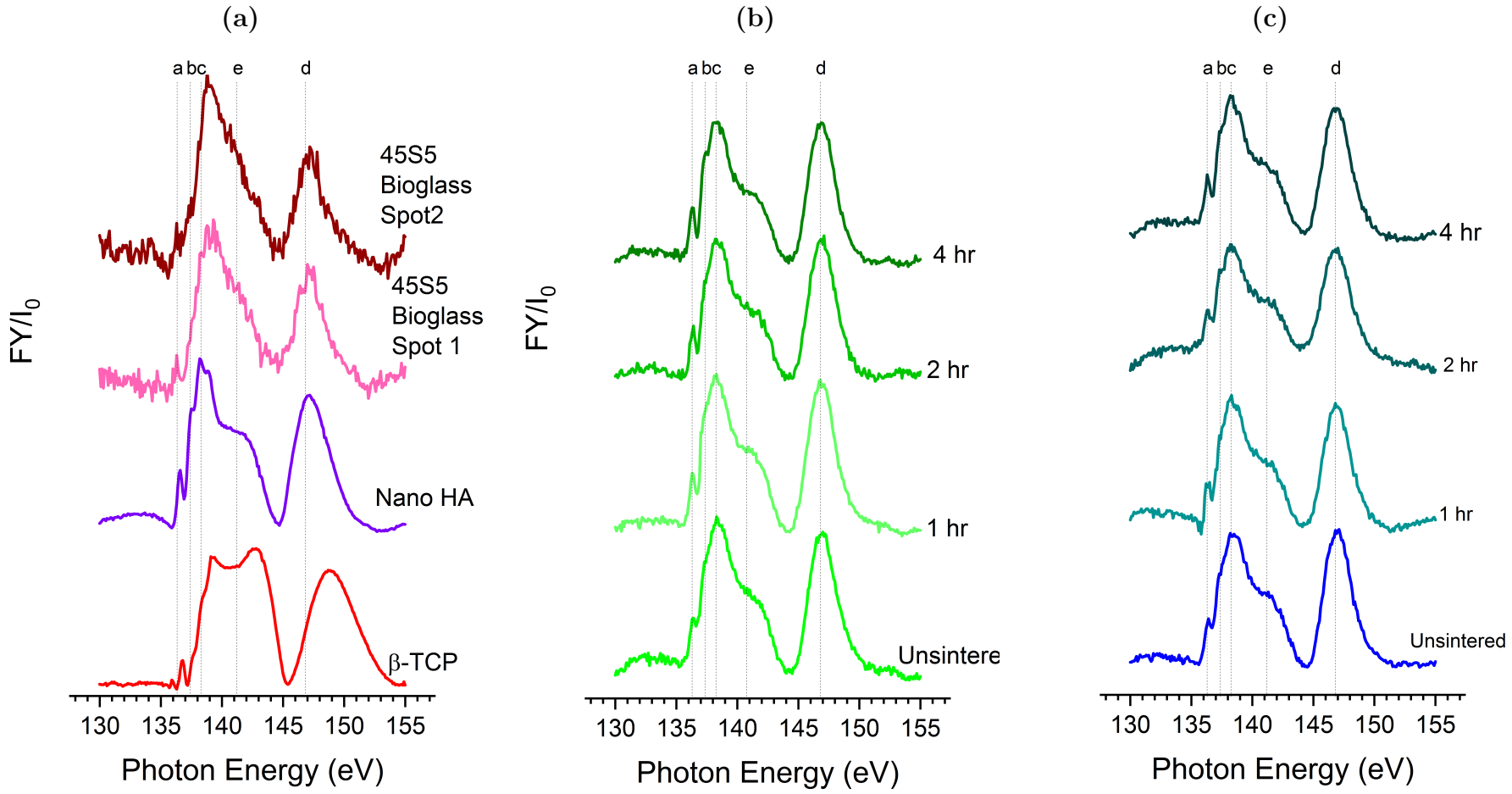

Figure 4.4: Phosphorus $L_{2,3}$-edge (a) Model Compounds (b) Gelatin Binder (c) Laponite Binder

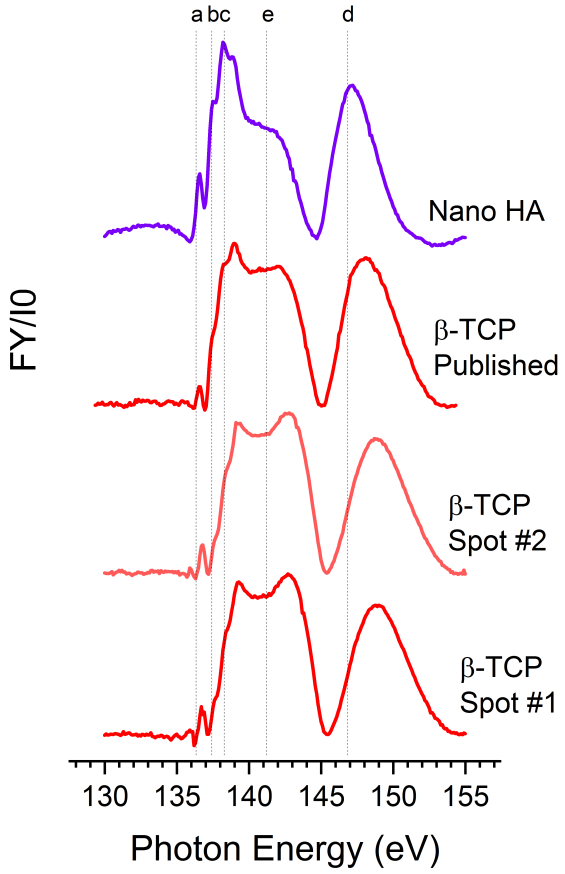

Figure 4.5: Phosphorus $L_{2,3}$-edge of β-TCP data from this study versus published data [2] and HA nanopowder

4.3.4 XANES Oxygen K-edge

The 30%BG + 70%β-TCP samples are similar to the Bioglass and β-TCP model compounds except they have a very prominent pre-edge peak B and post-edge shoulder E which both correspond with sodium silicate peaks.

The pre-edge for the sodium silicate is a doublet due to differences in the transition energy for non-bridging oxygen bond (Peak A) and bridging oxygen (Peak B). The 30%BG + 70%β-TCP samples do not have a prominent peak A, which indicates most of the silicon to oxygen bonding is bridging oxygen. The decrease in Peak A

is likely due to a combination of Na^+ dissolution from the Bioglass and preferential bonding of the NBO to Ca in the glass network.

The ratio between the peak heights for peaks B and D were calculated for the samples and any model compounds with corresponding peaks within 0.5 eV of the samples (Fig. 4.7). For both the laponite and gelatin samples, sintering reduced the height of the pre-edge peak B and the B/D peak ratio, but there was little difference between the 3 different sintering dwell times. This indicates that there is a reduction in BO bonding upon sintering.

The peak positions of the nanopowder and amorphous SiO_2 don't correspond with each other. Silica has several different polymorphs and the main peak is known to shift due to different oxygen bond angles [56].

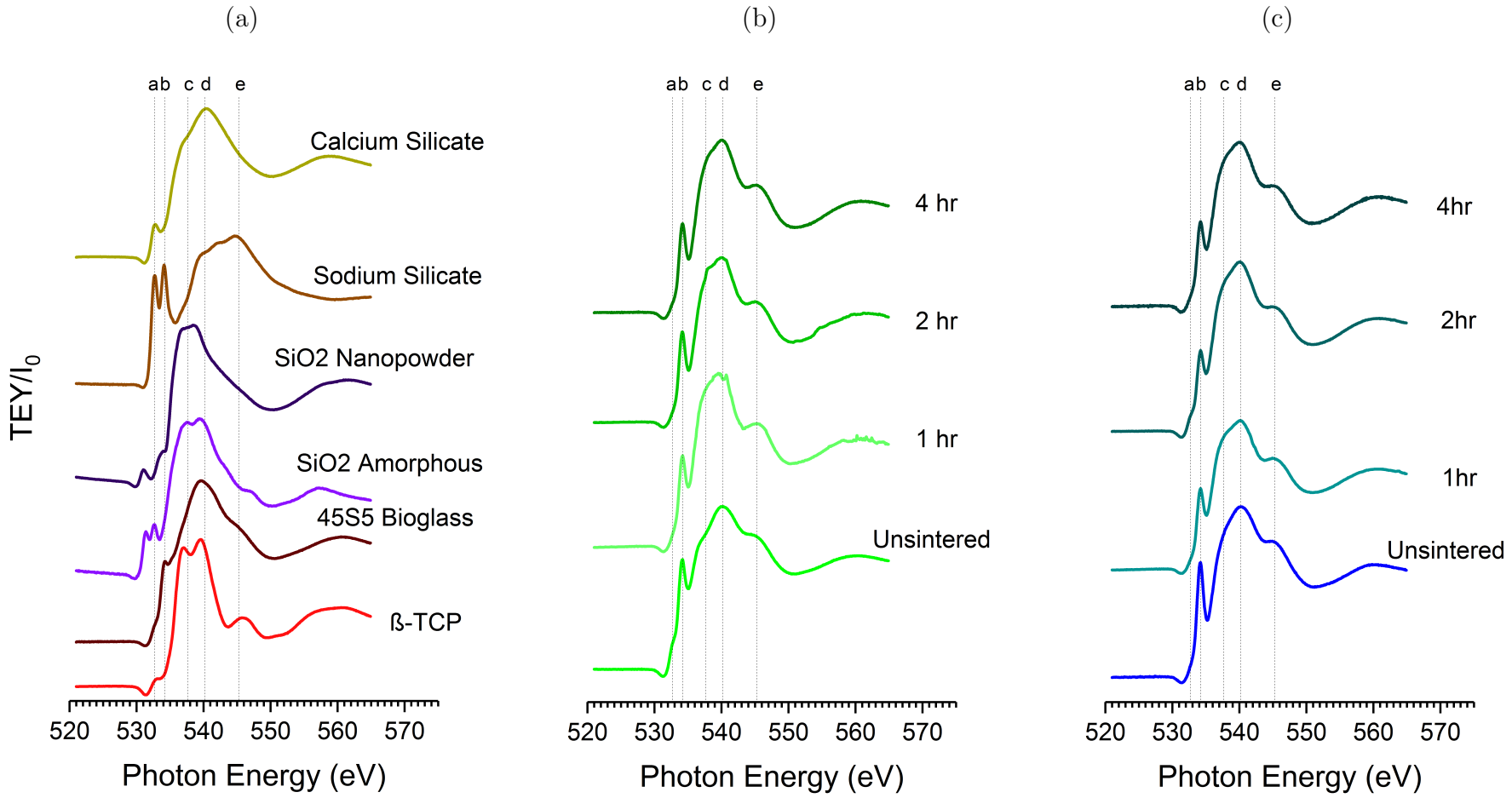

Figure 4.6: Oxygen K-edge (a) Model Compounds (b) Gelatin Binder (c) Laponite Binder

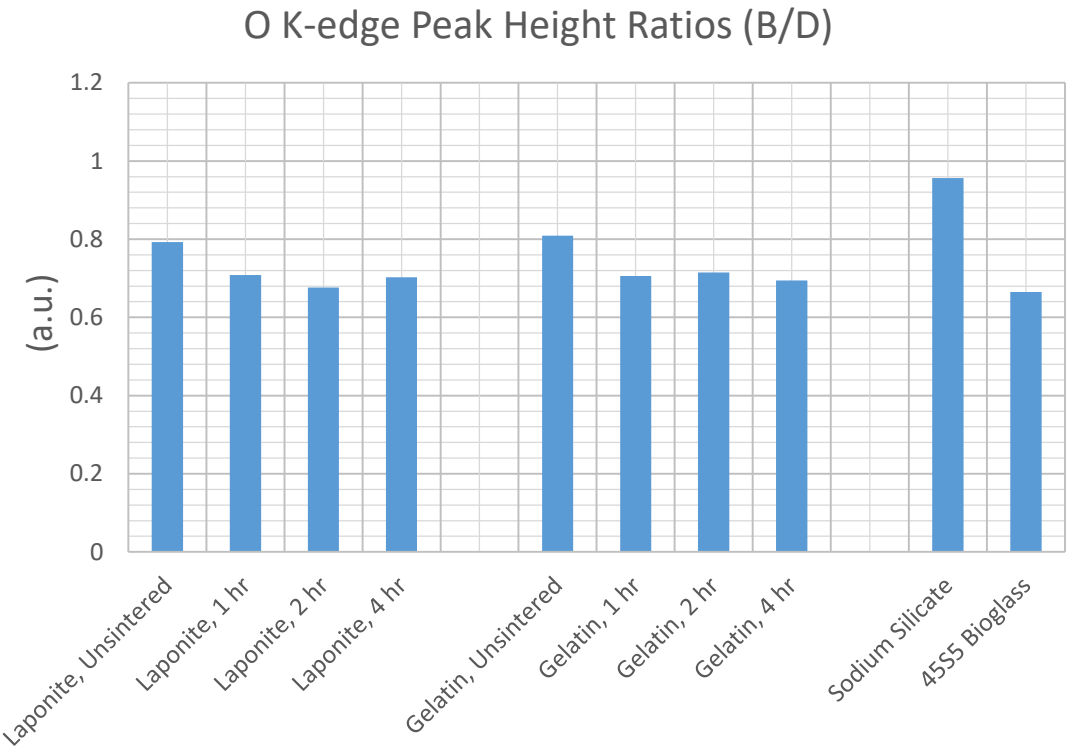

Figure 4.7: Ratio of B/D peak heights for samples and applicable model compounds

4.4 Conclusion

The XANES data shows that there are chemical changes to the oxygen bonding upon sintering, but the chemical activity primarily occurs with silicon bonding which changes throughout the sintering process.

The silicon $L_{2,3}$-edge shows a clear trend in the change in the bond structure for the laponite binder samples, but not the gelatin binder samples which indicates that the laponite is acting as an aid to improve the sintering process. This correlates with the increased strength for compression test data from Section 3.3.3.3.

The phosphorus $L_{2,3}$-edge reveals a nanoscale amorphous HA surface layer on the samples which would improve the bio-mimetic properties of the scaffold. There

were no significant changes with the phosphorus chemical bonding which indicates the the phosphate group is not active in the sintering process.

The oxygen K-edge shows that all the samples show bonding similar to sodium silicate except having a single prominent pre-edge peak for bridging oxygen instead of a doublet for both bridging oxygen and non-bridging oxygen peaks. This may be caused by a combination of sodium dissolution from the glass network and by preferential bonding of non-bridging oxygen to calcium which leaves the glass network more slowly.

CHAPTER 5

Robocasting

5.1 Introduction

5.1.1 Robocasting

Robocasting is an additive manufacturing process where a liquid 'ink' such as a slurry or hydrogel is extruded through a nozzle or syringe along a computer numerically controlled tool path in order to build a final part layer-by-layer. Robocasting differs from fused filament fabrication/fused deposition modeling since there are no melting and solidification processes occurring.

Robocasting requires a relatively simple equipment set up and allows for processing materials at room temperature. It also avoids the use of a powder bed which requires a large amount of material which can be expensive to fill. A disadvantage is that it does not naturally provide a way to support overhanging material that can occur in more complicated geometries, but this can be accommodated by either printing secondary support structure in a removable material or by printing in a suspension capable of supporting the material.

The coordinate system of the machine is defined so that horizontal X and Y axes are parallel to the print bed and the vertical Z axis is perpendicular to the print bed [57]. Movements of the machine are controlled using the standard G-code protocol ubiquitous in numerically controlled subtractive machining equipment [58].

Raster in the context of additive manufacturing, refers to a single extruded strand of material. For robocasting, the minimum width possible for a single raster/strand is determined mainly by the minimum nozzle diameter, but the extruded material may

experience die swelling after it exits the nozzle. The width of the extruded raster drives the resolution/minimum feature size which is critical since tissue engineering scaffolds need hierarchical structure across a wide range of scales [59]. Since the designed target pore width is fixed based on biological requirements for cell growth, the minimum nozzle diameter limits the maximum macroporosity that can be achieved for the scaffold. Ideally for the biological function of the scaffold, the macroporisity should be maximized to allow a larger volume for cell growth and infiltration [60].

5.1.2 Ceramic Slurries

A slurry is defined as a mixture where insoluble solid particles are suspended in a liquid. The slurry composition may be characterized either by a powder/liquid ratio (P/L) or a volume percent solids loading. For robocasting, the rheological properties are extremely important. The slurry must be highly pseudeoplastic (shear-thinning) to flow smoothly while dispensing then solidify in place once shear stresses are removed [61]. After extrusion, the slurry must then hold its shape and have sufficient strength to support the weight of subsequent layers.

During the drying of ceramic green bodies, the evaporation of the liquid phase causes stresses in the green body. The evaporation creates a vapor pressure gradient due to the capillary action as the liquid phase exits the green body [62]. Uneven drying, but not necessarily the drying rate, can induce stresses exceeding the strength of the green body causing cracking to occur during drying, which may not be evident until sintering/firing [63]. For robocasting, some researchers print in a non-wetting oil bath to prevent issues with uneven drying [64].

5.1.3 Injectability

Injectability is the ratio of material that can be extruded from a syringe as defined by equation 5.1.

$$Injectability = \frac{m_{extrudate}}{m_{total}} \tag{5.1}$$

It is proposed that the remaining unextruded material is due to phase separation from the following mechanisms [65]:

1) Die-filtration at the needle causing the liquid phase to move faster than solid phases.

2) Filtration in the syringe barrel caused by pressure from the plunger redistributing solids.

3) Local suction at the barrel exit causing the powder to separate/dilate which then causes the liquid phase to be drawn into and fill the created voids; This is affected by the angle of the barrel exit (i.e. tapered vs. 90° corner causing a dead zone).

5.2 Final Robocasting Methods

5.2.1 Equipment

Sample fabrication was performed on a modified CNC router capable of syringe extrusion [66][67][68]. A 3 mL plastic syringe barrel with a luer lock and a 8.5 mm inner diameter was used. The syringe plunger was actuated by a stepper motor providing a displacement controlled extrusion.

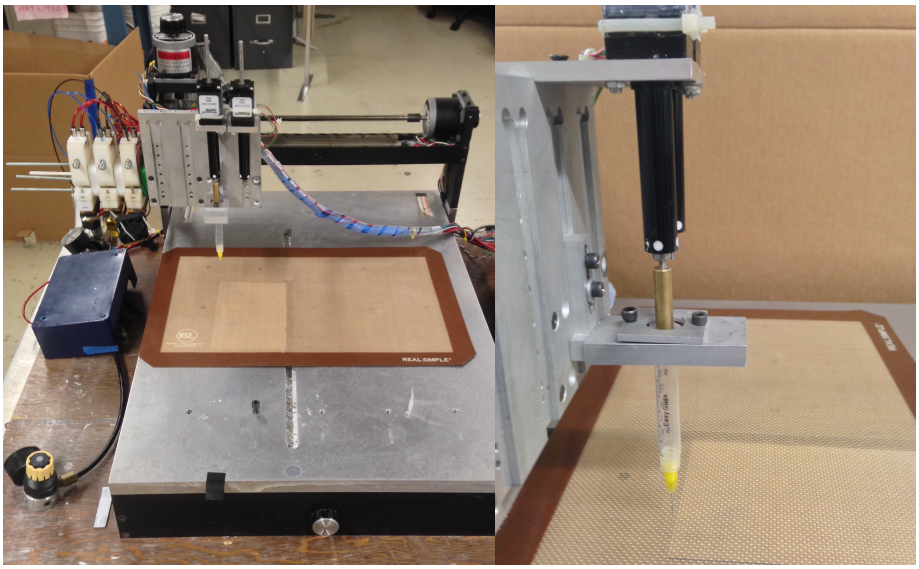

Figure 5.1: Bioplotter- Front and Side Views

5.2.2 Bed adhesion

Initial testing was performed on a print bed covered in blue painter's tape #2090 (3M, Saint Paul, Minnesota). The rough surface of the tape provided strong adhesion to the dried slurry, but the dried scaffolds were difficult to remove without damage. A silicone sheet (Weston Brands LLC, Independence, Ohio) was found to provide sufficient adhesion strength, while allowing the scaffolds to be easily removed with tweezers after drying.

5.2.3 Printing Parameters

The width of the extruded raster was assumed to be the diameter of the needle used (neglected die expansion). The needle used was a 20 gauge x 12.7 mm (0.5 inch) long blunt tip cannula needle with a 650 μm inner diameter, since it was the smallest needle that slurry could be extrude through reliably. In order to improve

bed adhesion and interlayer bonding, the layer height was set at 0.50 mm, which is 75% of the nominal raster width.

The speed of travel moves in the X and Y directions was 400 mm/min (i.e. while not extruding). The velocity of the syringe tip relative to the bed in the X and Y directions while printing is the write speed and had a value of 360 mm/min, which was determined by trial and error.

Due to capacitive effects of the slurry flow, there was a small delay in the stop and start of the flow during the printing process. A retraction process was used for brief pauses in the printing, where the plunger was retracted 0.05 mm at 600 mm/min. Since the plunger is displacement controlled, when the extrusion restarted, an additional length of 0.05 mm was provided to compensate for the retraction move and to ensure sufficient pressure.

5.2.4 Scaffold Geometry

The scaffolds were square with an overall dimension of 10 mm x 10 mm and a minimum height of 1.5 mm (3 layers). The raster infill pattern was a rectilinear crisscross pattern where the raster direction alternated between X and Y directions between layers (also known as wood-pile). The scaffolds had no perimeter rasters (i.e. no rasters followed along the edge of the scaffold) to increase the porosity. The sample macroporosity was defined by setting the infill density at 56.5% to obtain a target pore size of 300 μm.

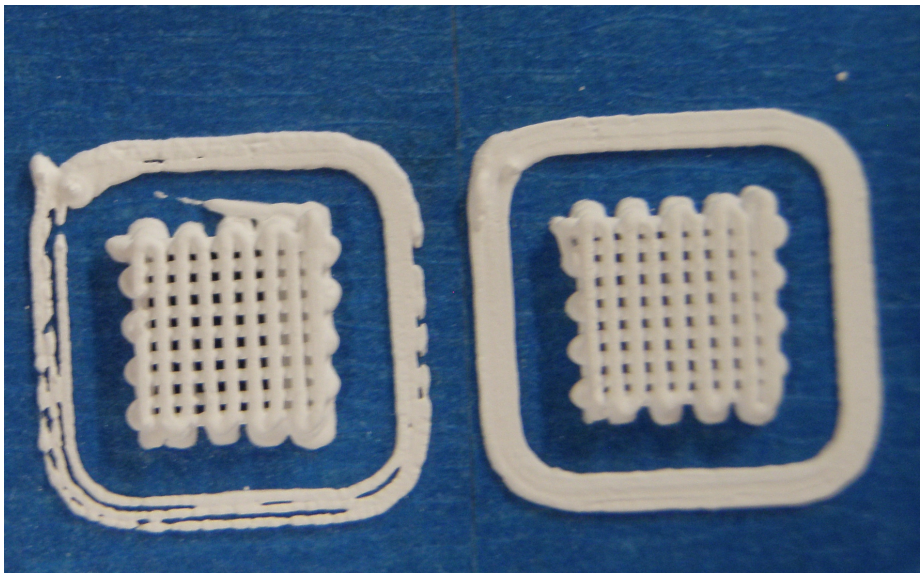

Figure 5.2: Top view of 10mm x 10mm robocasted scaffolds surrounded by two skirt loops

5.2.5 Scaffold Printing

Slurries were prepared per Chapter 2 Section 2.2.3 unless otherwise specified. Before calibrating the Z height of the needle, a small amount of slurry was purged out of the syringe to preload the syringe and extrusion mechanism. Initial flow of the slurry out of the needle was generally inconsistent so before printing the first layer of a scaffold, excess material was extruded in a skirt loop near the scaffold. After fabrication, the scaffolds were left to air dry at room temperature overnight.

5.3 Discussion of Issues Encountered

5.3.1 Printing Issues

The initial printing process produced scaffolds of extremely different quality between different tests with very poor repeatability (Fig. 5.3). Optimizing the printing parameters (print speed, layer height, etc.), generally improved the print quality

but did not fix repeatability issues, which was primarily an issue with the material. The results varied between different batches of the powder, different batches of the binders, and between different test days using the same batch of powders and binders.

The following problems were observed while robocasting:

1) Inconsistent flow leading to breaks in extrusion.
2) Uneven flow leading to under or over-extrusion.
3) Delay in flow restart at a layer change.
4) Loss of dimensional integrity after extrusion due to the flow of the extrudate (i.e. sagging of the layers or unintentional merging of the rasters).

(a)

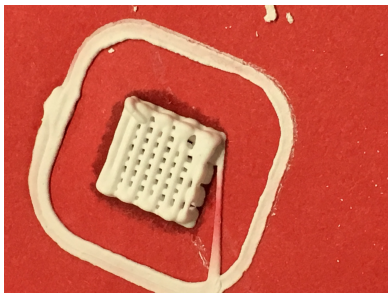

(b)

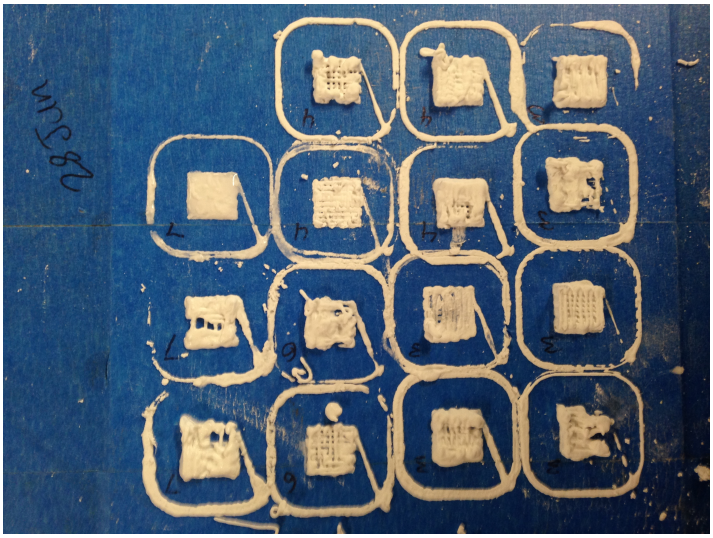

(c)

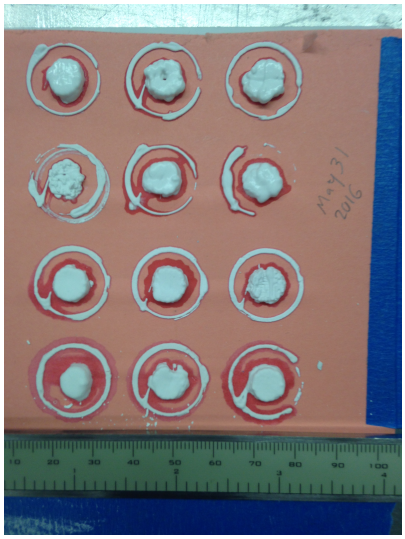

Figure 5.3: Results showing variations in early prints (a) Better quality print (b) Print quality ranging from failed to poor due to inconsistent uneven flow causing breaks over/under extrusions (c) Failed attempt at low macroporosity cylindrical scaffolds due to material flow after extrusion

5.3.2 Powder Processing

Contamination during ball milling was problematic. Both β-TCP and Bioglass react with water to form HA so water contamination is always a concern. The zirconia balls used as milling media tended to not dry completely after cleaning, which required the addition of a step to dry the milling media above 100°C. Over time the HDPE bottles used for milling would wear and become impregnated with ceramic phases. Using worn HDPE bottles had a significantly negative impact on the print quality, which requires the replacement of the bottles and potentially the milling media.

Issues with humidity and drying were investigated. Repeatability seemed to improve with more consistent drying times for removing the ethanol after ball milling. Secondary drying steps at 110°C were tested, but any mass loss during the process was negligible (less than 0.25%) which seems to indicate adsorption of water from ambient humidity wasn't a concern.

While the β-TCP powder particles are relatively small, the Bioglass particles are larger than other studies. Filtering the Bioglass particle by size is problematic. During a dry sieving process the powder tends to aggregate from vibration and during a wet filtration process in ethanol the filter becomes blocked by the formation of a thick cake of Bioglass particles. Other studies have successfully ball milled and sieved the Bioglass powders [69][70], and likely a higher energy milling process is needed (i.e. planetary mill or attrition mill).

5.3.3 Gelatin Binder

The gelatin binder system was initially modeled after an injectable cement application where in physiological conditions of 37°C the gelatin binder would not remain cross-linked since it exceeded the melting temperature of the gel. Also, when printing at room temperature the gelatin binder rheology is sensitive to the temperature, since

the operating temperature is near both the melting temperature and the gel point temperature, where the gel no longer flows [71].

The initial gelatin binder preparation process did not involve heating the sample and the lack of physical cross-linking decreased the print quality due to poor gel strength of the gelatin binder. This was easily rectified by heating the gelatin, and the preparation protocol for the Bloom test was chosen for consistency. Also the lack of a consistent gelatin temperature before mixing introduced variations in the printing process as the gelatin slowly warmed up to room temperature, and controlling the temperature greatly improved the repeatability.

5.3.4 Laponite Binder

The laponite binder consistently has a poorer print quality than the gelatin binder, and this is likely due to interactions between laponite gel network and the dissolution of Na^+ ions by the Bioglass and the low green body strength. Results varied based on the age of the binder and the repeatability was improved by implementing a mechanical mixing stage prior to use to break up age dependent gel phases.

The mechanical mixing did not improve the print quality itself, so the oleic acid was added as a surfactant. The phases of the laponite-water phase diagram are affected by salt concentration, which is problematic due to the dissolution of Na^+ ions from the Bioglass. The surfactant improved print quality for the laponite binder, but not for the gelatin binder, so the surfactant likely interferes more with the reactions between laponite and Na^+ ions than the Bioglass dissolution process.

5.3.5 Slurry Mixing and Syringe Loading

During the slurry mixing process, sometimes variations in the state of the binder caused the binder to not initially experience sufficient shear thinning and therefore unable to fully wet out the powder. Also in the initial mixing process, a small amount of ethanol (0.1 mL ethanol per 1 mL binder) was added as a mixing aid with the assumption that it would evaporate from the final mixture during the drying process. The ethanol introduced additional variability due to its rapid evaporation.

Inconsistent powder wet out led to the rejection of some slurry mixtures that may have been good as well as the addition of ethanol to 'fix' the slurry. Extending the minimum mixing time to at least 3 minutes consistently provides sufficient binder shear thinning to wet out the powder. This allowed for the removal of the ethanol which helps with the variability during printing. Mechanically mixing the slurry helps improve the consistency, but often the amount of slurry mixed was too small for mechanical mixing to be practical.

The slurries have a high viscosity and solid loading that requires packing the material into the syringe with a spatula. This introduces air pockets into the slurry, which can be reduced with careful loading of the syringe, but not eliminated. Injectability issues limit alternate loading methods that could eliminate the problem.

5.3.6 Syringe Setup

The reuse of syringe barrels caused repeatability problems, since after repeated use the plungers would require noticeably more load (hand force) to move through an empty syringe barrel. The cause is unknown and was not investigated due to the low cost of replacing syringes.

The 90 degree corner at the exit of the syringe barrel (above the luer lock) is a suspected contributor to poor injectability due to the suction at the barrel exit. This

study used smaller 3 mL syringes with an 8.5mm inner diameter, and therefore have a relatively small area reduction between the main barrel section and barrel exit when compared to larger syringes. This may be problematic when scaling up the process to larger quantities using larger diameter syringes. Syringe barrels with tapered exits are commercially available for pneumatically actuated plungers, but this would have required significant modification to our robocasting setup.

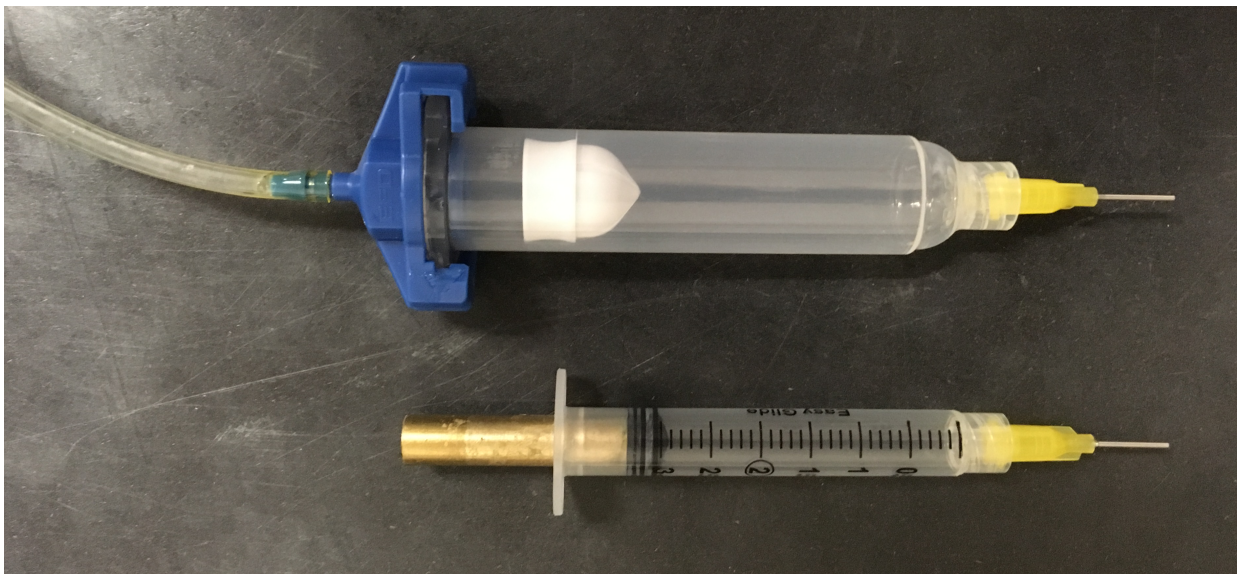

Figure 5.4: Syringe barrel types (Top) Nordson brand syringe with tapered barrel exit and (Bottom) standard 3mL syringe used in this study

5.3.7 Injectability

As previously discussed (Section 5.1.1), using a smaller needle is important for improving the function of the scaffolds. With the current powder and binder system, the slurry can be reliably extruded through a ∅650 μm diameter needle but only approximately 70% of the material can be extruded. Using a ∅200 μm needle with a 100% injectability would be more preferred.

The problem with a low percent injectability is that as the material is extruded during robocasting, the phases separate which changes the rheology of the mixture. The solid material that separates out increases the force required on the plunger until it eventually prevents consistent slurry flow out of the syringe

The binders when used with β-TCP without Bioglass or with fumed silica nanoparticles create slurries that do not have significant injectability issues, and the injectability problems are driven primarily by the interaction between Bioglass and water in the binder. Reducing the Bioglass particle size below 20μm by using wet filtration in ethanol with filter paper reduces the minimum needle size down to $\varnothing$410μm, but it does not improve the percent injectability.

As a proof of concept, the 30%Bioglass + 70%β-TCP powder was combined with a non-aqueous photopolymer resin and was successfully extruded through a $\varnothing$271 μm needle at a high percent injectability. The photopolymer used was an alphatic urethane acrylate (Solarez medium viscosity, Wahoo International, Vista, CA) and mixed with the powder at a P/L=1.25 ratio. The photopolymer is NOT biocompatible, but was chosen due to its commercial availability.

5.4 Conclusion

Robocasting has several benefits: a fairly simple and robust equipment setup, wide range of printing materials, and the ability to operate at room temperature. But robocasting is sensitive to the rheology, and small variations in the material can be very disruptive to the process, which can make it quite challenging. This requires a thorough understanding of the materials, especially the binders. Also improving the feature resolution requires decreasing the minimum needle diameter which is challenging for ceramic slurries due to issues with the separation of solid and liquid phases, which then worsens rheological problems.

CHAPTER 6

Conclusions and Recommendations for Future Work

6.1 Conclusions

At 500°C, there is some sintering occurring for the laponite binder samples. XANES oxygen K-edge data shows there is a slight reduction in the bridging oxygen bonds upon sintering. The silicon $L_{2,3}$-edge shows that there is change in the silicon bonding for longer sintering times, especially for the laponite binder samples. There is a 2.7 MPa increase in total strength of the laponite binder samples between the unsintered and 4 hr sinter dwell time, but there is no clear trend for the gelatin binder samples.

SEM images show sharp edges on the particles in the microstructure. Porosity analysis of the CT scan data shows little densification is occurring. This indicates that little diffusion is occurring and a higher temperature is needed to increase the diffusion rates to make the sintering process more effective.

XANES phosphorus $L_{2,3}$-edge data reveals that the hydroxyapatite formation has already begun during the slow drying process of the bulk samples. This is not visible with X-ray diffraction which indicates that this is a nanoscale amorphous surface layer of hydroxyapatite.

6.2 Recommendations for Future Work

If sintering at a higher temperature in the 600-670°C range proves effective, then improving the current powder-binder system may be preferable. Also, performing the PBS soak time test with sintered samples would evaluate how much further

strengthening would occur. Comparable β-TCP cement setting time tests show that a large percentage of the strengthening occurs before 28 days and sample soak times in the 14 to 21 day time frame should be examined [20][21][22].

For robocasting, a higher energy ball milling system will be needed to reduce the Bioglass particle size (i.e. planetary mill or attrition mill). The laponite binder needs several improvements. First, the green body strength of the slurry needs to be improved to help prevent drying cracks. The quality of the robocasted scaffolds needs to be improved in general for the laponite binder, and a better or more optimized surfactant may help the rheology.

Another alternative is using mesoporous bioactive glasses (MBG) which contain pores in the 2-50 nm range and are synthesized using a sol-gel process. It has been shown that crystalline mesoporous 45S5 Bioglass has comparable bioactivity to amorphous bulk 45S5 Bioglass and this bioactivity is attributed to the high surface area of the particles [72]. This would allow sintering at temperatures higher than the Bioglass crystallization temperature while still using the current chemical composition. Also there is greater flexibility with the chemical composition of the MBG. Sodium in bulk Bioglass lowers the melting temperature which aids in using a melt-quench synthesis process, and is also needed to help initiate the dissolution process in water that leads to the formation of CDHA. Sodium free MBG particles have been shown to form HA nanocrystals when heat treated to 550°C [73]. Removing the sodium from the glass composition has potential to improve the injectability issues and rheological issues with the laponite binder.

A polymer matrix-ceramic particle composite system may likely be a better option both in general and for robocasting. The benefit of 30% BG + 70% β-TCP the powder composition are the biological properties, not the mechanical properties. The slow dissolution of β-TCP is more ideal biologically, but also means the strength-

ening from converting to HA will also be slow and not provide initial strength to the scaffold. A polymer-ceramic composite would benefit from the initial strength of the polymer and later-stage strength from the HA formation as the polymer biodegrades or bioresorbs. Evaluation of the in-vitro degradation characteristics would be required to check for formation of brushite (pH<4.2) vs CDHA (pH>4.2) due to acidic byproducts from the polymer.

Instead of using a binder, using a non-aqueous polymer (i.e. not a hydrogel during extrusion) would allow for the 30% BG + 70% β-TCP powder mixture to be extruded without initiating the dissolution reactions of the Bioglass and changing the zeta potentials of the suspended Bioglass particles. This should improve both the minimum possible nozzle diameter and the percent injectability.

For any robocasted system, the rheology needs to be thoroughly evaluated at the beginning of the research. Injectability tests should show high percent injectability and sufficiently small minimum possible needle diameters before proceeding. Rheology tests should then verify the mixture is properly pseudoplastic and that the rheology is not dependent on the time from mixing.

To summarize this work in regard to developing a new composite biomaterial for bone defect healing applications, the following points need to be considered. First, β-TCP is a preferred material for bone tissue engineering since in physiological conditions it slowly converts to HA at a rate similar to natural bone growth and the reaction is a cell mediated process. But due to the slow dissolution process, β-TCP does not have an inherent mechanism to provide the needed initial strength due to the slow HA formation. Second, sodium is active in the chemistry of the Bioglass, and is part of the dissolution mechanism that leads to the formation of a calcium deficient hydroxyapatite surface layer which improves the bioactivity. The Na^+ dissolution in water creates a tendency for the Bioglass particles to separate from the slurry which

limits the injectability. Laponite nanoparticles are known to be sensitive to salt concentrations in water and the Na^+ ions appear to negatively affect the rheology of the slurry when using the laponite binder due to a reduced pseudoplasticity. Third, the laponite binder aids the sintering process at 500°C, but at this temperature there is little diffusion occurring, which shows a higher temperature is needed. Crystallization of Bioglass degrade the biological properties by making it more bioinert, so the sintering profile needs to be chosen to minimize Bioglass crystallization. Therefore the findings of this work can provide a significant impact on the development of novel bioactive materials which can provide mechanical reinforcement to resorbable polymers or improve the bioactivity of implants.

REFERENCES

[1] C.-N. Yao, "Osteogenic differentiation in preosteoblast mc3t3-e1 cells induced by beta tricalcium phosphate bioglass composite," mathesis, University of Texas at Arlington, July 2016.

[2] M. Maginot, S. Lin, Y. Liu, B. Yuan, J. Q. Feng, and P. B. Aswath, "The in vivo role of dmp-1 and serum phosphate on bone mineral composition," *Bone*, vol. 81, pp. 602–613, dec 2015. [Online]. Available: http://dx.doi.org/10.1016/j.bone.2015.08.018

[3] J. C. Elliott, *Structure and Chemistry of the Apatites and Other Calcium Orthophosphates:*. Elsevier Science & Technology, 1994. [Online]. Available: http://www.ebook.de/de/product/14767687/j_c_elliott_structure_and_chemistry_of_the_apatites_and_other_calcium_orthophosphates.html

[4] A. S. Greenwald, D. Phil(Oxon), S. D. B. (MD), R. L. B. (MD), M. P. B. (MD), V. M. G. (MD), M. J. Y. (MD), and C. S. H. (BSC), "The evolving role of bone-graft subsitutes," ser. Orthopaedic Device Forum. American Acadamey of Orthopaedic Surgeons, Mar. 2010, american Acadamey of Orthopaedic Surgeons 77th Annual Meeting March 9-13, 2010 New Orleans, Louisiana.

[5] A. Kinaci, V. Neuhaus, and D. C. Ring, "Trends in bone graft use in the united states," *Orthopedics*, vol. 37, no. 9, pp. e783–e788, sep 2014.

[6] L. Tang and W. Hu, "Molecular determinants of biocompatibility," *Expert Review of Medical Devices*, vol. 2, no. 4, pp. 493–500, jul 2005.

[7] D. W. Hutmacher, "Scaffolds in tissue engineering bone and cartilage," *Biomaterials*, vol. 21, no. 24, pp. 2529–2543, dec 2000.

[8] Q. L. Loh and C. Choong, "Three-dimensional scaffolds for tissue engineering applications: Role of porosity and pore size," *Tissue Engineering Part B: Reviews*, vol. 19, no. 6, pp. 485–502, dec 2013.

[9] J. M. Sobral, S. G. Caridade, R. A. Sousa, J. F. Mano, and R. L. Reis, "Three-dimensional plotted scaffolds with controlled pore size gradients: Effect of scaffold geometry on mechanical performance and cell seeding efficiency," *Acta Biomaterialia*, vol. 7, no. 3, pp. 1009–1018, mar 2011.

[10] D. B. Burr and O. Akkus, "Chapter 1 - bone morphology and organization," in *Basic and Applied Bone Biology*, D. B. Burr and M. R. Allen, Eds. San Diego: Academic Press, 2014, pp. 3 – 25. [Online]. Available: http://www.sciencedirect.com/science/article/pii/B9780124160156000010

[11] J. M. Hughes, "Shedding light on bone material," *American Mineralogist*, vol. 99, no. 1, pp. 1–1, jan 2014.

[12] S. Sakai, T. Anada, K. TsuchiyaA, H. Yamazaki, H. C. Margolis, and O. Suzuki, "Comparative study on the resorbability and dissolution behavior of octacalcium phosphate, β-tricalcium phosphate, and hydroxyapatite under physiological conditions," *Dental Materials Journal*, vol. 35, no. 2, pp. 216–224, 2016.

[13] C. Migliaresi and A. Motta, *Scaffolds for Tissue Engineering: Biological Design, Materials, and Fabrication*, 1st ed., ser. Chapter 12, Venu G. Varanasi, Panayiotis S. Shiakolas, and Pranesh B. Aswath. Pan Stanford Publishing Pte Ltd, 2014.

[14] A. Martinez, O. Balboa, I. Gasamans, X. L. Otero-Cepeda, and F. Guitian, "Deproteinated bovine bone vs. beta-tricalcium phosphate as bone graft substitutes: histomorphometric longitudinal study in the rabbit cranial vault," *Clinical Oral Implants Research*, vol. 26, no. 6, pp. 623–632, feb 2014.

[15] N. S. Tousi, M. F. Velten, T. J. Bishop, K. K. Leong, N. S. Barkhordar, G. W. Marshall, P. M. Loomer, P. B. Aswath, and V. G. Varanasi, "Combinatorial

effect of si4 +, ca2 +, and mg2 + released from bioactive glasses on osteoblast osteocalcin expression and biomineralization," *Materials Science and Engineering: C*, vol. 33, no. 5, pp. 2757 – 2765, 2013. [Online]. Available: http://www.sciencedirect.com/science/article/pii/S0928493113001446

[16] J. Jones and A. Clare, *Bio-Glasses: An Introduction*. Wiley, May 2012.

[17] M. Akao, H. Aoki, K. Kato, and A. Sato, "Dense polycrystalline β-tricalcium phosphate for prosthetic applications," *Journal of Materials Science*, vol. 17, no. 2, pp. 343–346, feb 1982.

[18] J. Zhang, W. Liu, V. Schnitzler, F. Tancret, and J.-M. Bouler, "Calcium phosphate cements for bone substitution: Chemistry, handling and mechanical properties," *Acta Biomaterialia*, vol. 10, no. 3, pp. 1035–1049, mar 2014.

[19] M. Bohner, "Reactivity of calcium phosphate cements," *Journal of Materials Chemistry*, vol. 17, no. 38, p. 3980, 2007.

[20] N. Ahmad, K. Tsuru, M. L. Munar, M. Maruta, S. Matsuya, and K. Ishikawa, "Effect of precursor s solubility on the mechanical property of hydroxyapatite formed by dissolution-precipitation reaction of tricalcium phosphate," *Dental Materials Journal*, vol. 31, no. 6, p. 9951000, Aug. 2012.

[21] M. Ginebra, E. Fernandez, E. D. Maeyer, R. Verbeeck, M. Boltong, J. Ginebra, F. Driessens, and J. Planell, "Setting reaction and hardening of an apatitic calcium phosphate cement," *Journal of Dental Research*, vol. 76, no. 4, pp. 905–912, apr 1997.

[22] U. Gbureck, "Mechanical activation and cement formation of beta-tricalcium phosphate," *Biomaterials*, vol. 24, no. 23, pp. 4123–4131, oct 2003.

[23] L. L. Hench, "Chronology of bioactive glass development and clinical applications," *New Journal of Glass and Ceramics*, vol. 03, no. 02, pp. 67–73, 2013. [Online]. Available: http://dx.doi.org/10.4236/njgc.2013.32011

[24] A. Hoppe, N. S. Gldal, and A. R. Boccaccini, "A review of the biological response to ionic dissolution products from bioactive glasses and glass-ceramics," *Biomaterials*, vol. 32, no. 11, pp. 2757–2774, apr 2011.

[25] S. Eqtesadi, A. Motealleh, P. Miranda, A. Lemos, A. Rebelo, and J. M. Ferreira, "A simple recipe for direct writing complex 45s5 bioglass 3d scaffolds," *Materials Letters*, vol. 93, pp. 68 – 71, feb 2013. [Online]. Available: http://www.sciencedirect.com/science/article/pii/S0167577X12016072

[26] S. Eqtesadi, A. Motealleh, P. Miranda, A. Pajares, A. Lemos, and J. M. Ferreira, "Robocasting of 45s5 bioactive glass scaffolds for bone tissue engineering," *Journal of the European Ceramic Society*, vol. 34, no. 1, pp. 107–118, jan 2014.

[27] Q. Z. Chen, A. Efthymiou, V. Salih, and A. R. Boccaccini, "Bioglass®-derived glass–ceramic scaffolds: Study of cell proliferation and scaffold degradationin vitro," *Journal of Biomedical Materials Research Part A*, vol. 84A, no. 4, pp. 1049–1060, 2008.

[28] H. Babin and E. Dickinson, "Influence of transglutaminase treatment on the thermoreversible gelation of gelatin," *Food Hydrocolloids*, vol. 15, no. 3, pp. 271–276, may 2001.

[29] L. S. Nair and C. T. Laurencin, "Polymers as biomaterials for tissue engineering and controlled drug delivery," in *Tissue Engineering I.* Springer Nature, 2005, pp. 47–90.

[30] Z. Zha, W. Teng, V. Markle, Z. Dai, and X. Wu, "Fabrication of gelatin nanofibrous scaffolds using ethanol/phosphate buffer saline as a benign solvent," *Biopolymers*, vol. 97, no. 12, pp. 1026–1036, sep 2012.

[31] M. Gmez-Guilln, B. Gimnez, M. Lpez-Caballero, and M. Montero, "Functional and bioactive properties of collagen and gelatin from alternative sources: A review," *Food Hydrocolloids*, vol. 25, no. 8, pp. 1813 – 1827, 2011,

25 years of Advances in Food Hydrocolloid Research. [Online]. Available: http://www.sciencedirect.com/science/article/pii/S0268005X11000427

[32] *Standard Testing Methods for Edible Gelatin*, Gelatin Manufactures Institute of America Std., July 2013. [Online]. Available: http://www.gelatin-gmia.com/images/GMIA_Official_Methods_of_Gelatin_Revised_2013.pdf

[33] X. Zhai, Y. Ma, C. Hou, F. Gao, Y. Zhang, C. Ruan, H. Pan, W. W. Lu, and W. Liu, "3d-printed high strength bioactive supramolecular polymer/clay nanocomposite hydrogel scaffold for bone regeneration," *ACS Biomaterials Science & Engineering*, vol. 3, no. 6, pp. 1109–1118, May 2017.

[34] H. Z. Cummins, "Liquid, glass, gel: The phases of colloidal laponite," *Journal of Non-Crystalline Solids*, vol. 353, no. 4143, pp. 3891 – 3905, nov 2007, in Honour of Kia L. NgaiSelected papers from the symposium in honour of Kia L. NgaiSymposium in Honour of Kia L. Ngai. [Online]. Available: //www.sciencedirect.com/science/article/pii/S0022309307007612

[35] B. Ruzicka and E. Zaccarelli, "A fresh look at the laponite phase diagram," *Soft Matter*, vol. 7, no. 4, p. 1268, 2011.

[36] M. Julien, J. M. Hoeffel, and M. R. Flick, "Oleic acid lung injury in sheep," *Journal of Applied Physiology*, p. 433, 1985.

[37] *Safety Data Sheet*, 4th ed., Sigma-Aldrich, Nov. 2016, product name : Oleic acid Product Number : 364525 Brand : Aldrich CAS-No. : 112-80-1. [Online]. Available: http://www.sigmaaldrich.com/MSDS/MSDS/DisplayMSDSPage.do?country=US&language=en&productNumber=364525&brand=ALDRICH

[38] *Standard Test Method for Monotonic Compressive Strength of Advanced Ceramics at Ambient Temperature*, ASTM International Std. ASTM C1424, 2015.

[39] *Standard Test Method for Compressive (Crushing) Strength of Fired Whiteware Materials*, ASTM International Std. ASTM C773, 2016.

[40] C. B. Carter and M. G. Norton, *Ceramic Materials: Science and Engineering*. Springer, 2007. [Online]. Available: https://www.amazon.com/Ceramic-Materials-Engineering-Barry-Carter/dp/0387462708?SubscriptionId=0JYN1NVW651KCA56C102&tag=techkie-20&linkCode=xm2&camp=2025&creative=165953&creativeASIN=0387462708

[41] C. Bergmann, M. Lindner, W. Zhang, K. Koczur, A. Kirsten, R. Telle, and H. Fischer, "3d printing of bone substitute implants using calcium phosphate and bioactive glasses," *Journal of the European Ceramic Society*, vol. 30, no. 12, pp. 2563–2567, sep 2010.

[42] J. H. Lopes, J. A. Magalhes, R. F. Gouveia, C. A. Bertran, M. Motisuke, S. E. Camargo, and E. de Sousa Trichs, "Hierarchical structures of -tcp/45s5 bioglass hybrid scaffolds prepared by gelcasting," *Journal of the Mechanical Behavior of Biomedical Materials*, vol. 62, pp. 10 – 23, 2016. [Online]. Available: http://www.sciencedirect.com/science/article/pii/S1751616116300923

[43] L. Desogus, A. Cuccu, S. Montinaro, R. Orrù, G. Cao, D. Bellucci, A. Sola, and V. Cannillo, "Classical bioglass and innovative cao-rich bioglass powders processed by spark plasma sintering: A comparative study," *Journal of the European Ceramic Society*, vol. 35, no. 15, pp. 4277–4285, dec 2015. [Online]. Available: //www.sciencedirect.com/science/article/pii/S0955221915300686

[44] X. Zhang, Q. Cai, H. Liu, S. Zhang, Y. Wei, X. Yang, Y. Lin, Z. Yang, and X. Deng, "Calcium ion release and osteoblastic behavior of gelatin/beta-tricalcium phosphate composite nanofibers fabricated by electrospinning," *Materials Letters*, vol. 73, pp. 172–175, apr 2012.

[45] I. Ascone, "X-ray absorption spectroscopy for beginners," in *IUCr 2011 XAFS Tutorial*, ser. IUCr 2011 XAFS Tutorial. International Union of

Crystallography, 2011. [Online]. Available: http://www.iucr.org/__data/assets/pdf_file/0004/60637/IUCr2011-XAFS-Tutorial_-Ascone.pdf

[46] J. Yano and V. K. Yachandra, "X-ray absorption spectroscopy," *Photosynthesis Research*, vol. 102, no. 2-3, pp. 241–254, aug 2009.

[47] J. Cosmidis, K. Benzerara, N. Nassif, T. Tyliszczak, and F. Bourdelle, "Characterization of ca-phosphate biological materials by scanning transmission x-ray microscopy (stxm) at the ca $l_{2,3}$-, p $l_{2,3}$- and c k-edges," *Acta Biomaterialia*, vol. 12, pp. 260–269, Jan. 2015.

[48] J. Rajendran, S. Gialanella, and P. B. Aswath, "XANES analysis of dried and calcined bones," *Materials Science and Engineering: C*, vol. 33, no. 7, pp. 3968–3979, oct 2013.

[49] O. O. Aruwajoye, H. K. W. Kim, and P. B. Aswath, "Bone apatite composition of necrotic trabecular bone in the femoral head of immature piglets," *Calcified Tissue International*, vol. 96, no. 4, pp. 324–334, feb 2015.

[50] H. Demirkiran, Y. Hu, L. Zuin, N. Appathurai, and P. B. Aswath, "XANES analysis of calcium and sodium phosphates and silicates and hydroxyapatite–bioglass®45s5 co-sintered bioceramics," *Materials Science and Engineering: C*, vol. 31, no. 2, pp. 134–143, mar 2011.

[51] A. Mekki, G. Khattak, D. Holland, M. Chinkhota, and L. Wenger, "Structure and magnetic properties of vanadium–sodium silicate glasses," *Journal of Non-Crystalline Solids*, vol. 318, no. 1-2, pp. 193–201, apr 2003. [Online]. Available: https://doi.org/10.1016/S0022-3093(02)01883-5

[52] P. Onorato, M. Alexander, C. Struck, W. Tasker, and D. Uhlmann, "Bridging and nonbridging oxygen atoms in alkali aluminosilicate glasses," *Journal of the American Ceramic Society*, 1985.

[53] V. Petkov, S. J. L. Billinge, S. D. Shastri, and B. Himmel, "Polyhedral units and network connectivity in calcium aluminosilicate glasses from high-energy x-ray diffraction," *Physical Review Letters*, vol. 85, no. 16, pp. 3436–3439, oct 2000. [Online]. Available: https://doi.org/10.1103/PhysRevLett.85.3436

[54] L. Cormier and D. Neuville, "Ca and na environments in na2o–CaO–al2o3–SiO2 glasses: influence of cation mixing and cation-network interactions," *Chemical Geology*, vol. 213, no. 1-3, pp. 103–113, dec 2004. [Online]. Available: https://doi.org/10.1016/j.chemgeo.2004.08.049

[55] *Specification for Beta-Tricalcium Phosphate for Surgical Implantation*, ASTM International Std. ASTM F1088, 2010.

[56] I. Davoli, E. Paris, S. Stizza, M. Benfatto, M. Fanfoni, A. Gargano, A. Bianconi, and F. Seifert, "Structure of densified vitreous silica: Silicon and oxygen XANES spectra and multiple scattering calculations," *Physics and Chemistry of Minerals*, vol. 19, no. 3, sep 1992.

[57] *Standard Practice for Reporting Data for Test Specimens Prepared by Additive Manufacturing*, ASTM International Std. ASTM F2971, 2013.

[58] T. R. Kramer, F. M. Proctor, and E. Messina, *The NIST RS274NGC Interpreter*, National Institute of Standards and Technology Std. NISTIR 6556, Rev. Version 3, Aug. 2000.

[59] S. J. Hollister, "Hierarchical bioactive materials for tissue reconstruction: Integrated design and manufacturing challenges," *JOM*, vol. 63, no. 4, pp. 56–65, apr 2011.

[60] M. R. Dias, J. M. Guedes, C. L. Flanagan, S. J. Hollister, and P. R. Fernandes, "Optimization of scaffold design for bone tissue engineering: A computational and experimental study," *Medical Engineering & Physics*, vol. 36, no. 4, pp. 448–457, apr 2014.

[61] J. Cesarano, III, R. Segalman, and P. Calvert, "Robocasting provides moldless fabrication from slurry deposition," *Ceramic Industry*, vol. 148, no. 4, pp. 94–102, 04 1998, copyright - Copyright Business News Publishing Company Apr 1998; Last updated - 2014-05-22; CODEN - CEINAT. [Online]. Available: http://search.proquest.com/docview/198566608?accountid=7117

[62] T. A. Ring, *Fundamentals of Ceramic Powder Processing and Synthesis*. Elsevier Science, 1996, no. Chapter 14. [Online]. Available: http://www.sciencedirect.com/science/book/9780125889308

[63] T. Hansen, "The black art of drying ceramics without cracks," 2003, accessed March 2017. [Online]. Available: https://digitalfire.com/4sight/education/the_black_art_of_drying_ceramics_without_cracks_196.html

[64] F. J. Martínez-Vázquez, F. H. Perera, P. Miranda, A. Pajares, and F. Guiberteau, "Improving the compressive strength of bioceramic robocast scaffolds by polymer infiltration," *Acta Biomaterialia*, vol. 6, no. 11, pp. 4361–4368, nov 2010.

[65] R. O'Neill, H. O. McCarthy, E. Cunningham, E. Montufar, M.-P. Ginebra, D. I. Wilson, A. Lennon, and N. Dunne, "Extent and mechanism of phase separation during the extrusion of calcium phosphate pastes," *Journal of Materials Science: Materials in Medicine*, vol. 27, no. 2, dec 2015.

[66] P. Ravi, P. S. Shiakolas, T. Welch, T. Saini, K. Guleserian, and A. K. Batra, "On the capabilities of a multi-modality 3d bioprinter for customized biomedical devices," in *Volume 2A: Advanced Manufacturing*. ASME, Nov. 2015.

[67] P. Ravi, P. S. Shiakolas, J. C. Oberg, S. Faizee, and A. K. Batra, "On the development of a modular 3d bioprinter for research in biomedical device fabrication," in *Volume 2A: Advanced Manufacturing*. ASME, nov 2015.

[68] P. Ravi, P. S. Shiakolas, and A. D. Thorat, "Analyzing the effects of temperature, nozzle-bed distance, and their interactions on the width of fused deposition modeled struts using statistical techniques toward precision scaffold fabrication," *Journal of Manufacturing Science and Engineering*, vol. 139, no. 7, p. 071007, mar 2017.

[69] T. Long, J. Yang, S.-S. Shi, Y.-P. Guo, Q.-F. Ke, and Z.-A. Zhu, "Fabrication of three-dimensional porous scaffold based on collagen fiber and bioglass for bone tissue engineering," *Journal of Biomedical Materials Research Part B: Applied Biomaterials*, vol. 103, no. 7, pp. 1455–1464, nov 2014.

[70] S.-C. Wu, H.-C. Hsu, S.-H. Hsiao, and W.-F. Ho, "Preparation of porous 45s5 bioglass®-derived glass–ceramic scaffolds by using rice husk as a porogen additive," *Journal of Materials Science: Materials in Medicine*, vol. 20, no. 6, pp. 1229–1236, jan 2009.

[71] F. A. Osorio, E. Bilbao, R. Bustos, and F. Alvarez, "Effects of concentration, bloom degree, and pH on gelatin melting and gelling temperatures using small amplitude oscillatory rheology," *International Journal of Food Properties*, vol. 10, no. 4, pp. 841–851, oct 2007.

[72] H. Pirayesh and J. A. Nychka, "Sol-gel synthesis of bioactive glass-ceramic 45s5 and itsin vitroDissolution and mineralization behavior," *Journal of the American Ceramic Society*, vol. 96, no. 5, pp. 1643–1650, Feb 2013.

[73] G. Melinte, L. Baia, V. Simon, and S. Simon, "Hydrogen peroxide versus water synthesis of bioglass–nanocrystalline hydroxyapatite composites," *Journal of Materials Science*, vol. 46, no. 23, pp. 7393–7400, Dec 2011. [Online]. Available: https://doi.org/10.1007/s10853-011-5700-8

BIOGRAPHICAL STATEMENT

Phillip Zachary James received his B.S. in Mechanical Engineering from Texas Tech University in 2007. He spent 8 years working as a mechanical engineer designing aerospace tooling at L3 Communications Mission Integration Division in Greenville, Texas. In 2015, he started his M.S. degree in Material Science and Engineering at the Univeristy of Texas at Arlington and completed his thesis work in 2017.

His area of expertise include composite and assembly tooling, CAD design and drafting, and geometric dimensioning and tolerancing. His technical interest include additive manufacturing, 3D scanning, and other manufacturing processes.